Sustainable Cities and Society 135 (2025) 106981

Contents lists available at ScienceDirect

Sustainable Cities and Society

journal homepage: www.elsevier.com/locate/scs

High-resolution carbon modeling in dense urban areas: LiDAR-validated spatiotemporal mapping for neighborhood decarbonization

Yueyue Wu [a,b,c,1], Yi Zheng [b,d,1], Yixiang Chen [e,f], Xinbei Wang [c], Zhen Zhang [e,f,g], Saifen Yu [e,f,g], Haiyun Xia [e,f,g,h], ChengHe Guan [c,i,*]

[a] Collective Intelligence and Design Group, University of Cambridge, Cambridge CB2 1PX, UK
[b] School of Architecture, Southeast University, Nanjing 210096, China
[c] Shanghai Key Laboratory of Urban Design and Urban Science, NYU Shanghai, 567 West Yangsi Road, Pudong New District, Shanghai 200122, China
[d] Key Laboratory of Ecology and Energy Saving Study of Dense Habitat, Ministry of Education, Shanghai 200092, China
[e] State Key Laboratory of Climate System Prediction and Risk Management, Nanjing University of Information Science and Technology, Nanjing 210044, China
[f] School of Atmospheric Physics, Nanjing University of Information Science and Technology, Nanjing 210044, China
[g] National Center of Carbon Metrology (Fujian), Nanping 353000, China
[h] School of Earth and Space Science, University of Science and Technology of China, Heife 230026, China
[i] Division of Arts and Sciences, NYU Shanghai, Shanghai 200122, China

ARTICLE INFO

Keywords:
Spatiotemporal carbon emission model
Carbon accounting
Neighborhood decarbonization
Dense cities carbon neutrality

ABSTRACT

Accurate and actionable carbon emission accounting is critical for sustainable transformation in high-density urban environments and for meeting global climate change mitigation targets. However, conventional approaches lack both fine spatiotemporal resolution and robust ground validation. To address this gap, this study develops a machine learning-optimized Spatiotemporal Carbon Emission Model (SCE-Model) that integrates multi-source urban datasets to produce hourly, neighborhood-scale carbon emission maps for Nanjing Old City, China. Model output demonstrates strong agreement with coherent differential absorption LiDAR (CDIAL) observations ($R^2 = 0.79$; ±5 ppm). Key findings include: (1) Human metabolic activity constitutes the predominant source of CO_2 emissions (6.17 million kg/day), surpassing building operations (0.84 million kg/day) and transportation (1.05 million kg/day). The two primary anthropogenic sources exhibit distinct diurnal rhythms and spatial clustering, driving the formation of emission hotspots. (2) Urban green spaces provide a significant carbon sink, although they offset only approximately 0.6 % of gross anthropogenic emissions. (3) Five neighborhood emission typologies are identified to enable spatially targeted decarbonization strategies, including low-emission, building-dominated, mixed high-emission, transportation-dominated, and high carbon-sink. The proposed framework provides a high-resolution carbon accounting method for dense cities, offering a scientific basis for targeted neighborhood decarbonization strategies. This work advances the scientific foundation for integrating anthropogenic emissions, urban green spaces, and neighborhood typology into next-generation urban carbon management policies, contributing to the goal of achieving urban carbon neutrality.

1. Introduction

Urban areas accounted for over 70 % of global CO_2 emissions in 2022, with high-density cities facing intensified decarbonization pressures due to concentrated energy demand, traffic congestion, and limited green space (UN-Habitat, 2022). By 2050, 68 % of the global population will reside in urban areas—including 43 megacities exceeding 10 million inhabitants—making these hyper-dense cores critical carbon hotspots requiring urgent intervention to meet net-zero targets (IPCC, 2022; Mi et al., 2019). Addressing carbon goals in these high-density environments requires refinements in the accuracy and spatial granularity of urban carbon accounting.

* Corresponding author.
E-mail addresses: yw837@cam.ac.uk (Y. Wu), yizheng@seu.edu.cn (Y. Zheng), 202411050001@nuist.edu.cn (Y. Chen), xw3147@nyu.edu (X. Wang), 003514@nuist.edu.cn (Z. Zhang), sfyu@nuist.edu.cn (S. Yu), hsia@ustc.edu.cn (H. Xia), cg157@nyu.edu (C. Guan).
[1] These authors contributed equally to this work.

https://doi.org/10.1016/j.scs.2025.106981
Received 4 September 2025; Received in revised form 10 November 2025; Accepted 11 November 2025
Available online 12 November 2025

However, existing carbon accounting frameworks are not well-suited for neighborhood-scale planning. Top-down methods (e.g., IPCC inventories, NTL-based downscaling) often operate at coarse resolutions (>1 km^2, annual), obscuring critical neighborhood-level variations and hourly emission spikes (Brown & MacAskill, 2025; Ye et al., 2025). While bottom-up inventories offer finer detail, they are often data-intensive, sector-specific, and seldom integrate non-traditional sources like human metabolism or urban carbon sinks, nor are they typically validated against high-resolution, spatially representative empirical observations. (Winbourne et al., 2022; Ye et al., 2023). To address these gaps, this study develops a machine learning-enhanced Spatiotemporal Carbon Emission Model (SCE-Model) that integrates multi-source urban data, including traffic flows, building energy consumption, human mobility patterns, and vegetation dynamics. Coherent Differential Absorption LiDAR (CDIAL) provides fine-grained in situ CO_2 concentration measurements, which are used to validate the model. The methodology is demonstrated in Nanjing Old City, China, enabling hourly carbon emission estimation at the neighborhood scale with improved spatial and temporal detail.

This research aims to address the following questions: (1) How can a unified modeling framework validate and enable carbon emissions accounting at hourly, neighborhood-scale resolution? (2) What are the spatiotemporal patterns of carbon emissions in high-density urban areas? (3) How can high-resolution emission data inform neighborhood typologies and guide targeted decarbonization strategies?

This work makes several contributions to advance the state of the art. First, the establishment of a high-resolution mapping framework. It establishes hourly carbon emission mapping at the neighborhood scale, which is essential for understanding intricate emission dynamics and identifying the underlying drivers that are often obscured in macro-level analyses. Second, the introduction of a novel validation approach. To ground the insights in empirical reality, we demonstrate the use of near-surface CDIAL measurements to provide a high-precision, spatially representative benchmark at the urban canopy level, complementing existing satellite observations and point-based measurements. Finally, the development of actionable decision support through neighborhood typologies. By translating these data into actionable intelligence, the study enables a shift from generalized policy to targeted action.

The remainder of this paper is organized as follows: Section 2 reviews relevant literature on carbon accounting methods in dense urban areas and sensor-based validation approaches; Section 3 details the proposed framework, including four sub-models for buildings, traffic, human metabolism, and carbon sinks, with CDIAL validation methodology; Section 4 reports the modeling and validation results; Section 5 discusses spatiotemporal patterns of carbon emissions, implications for decarbonization, and limitations. Section 6 summarizes conclusions and outlines future work.

2. Literature review

2.1. Carbon emission accounting in high-density urban areas

Urban carbon accounting forms the quantitative foundation for decarbonization strategies in cities. Existing approaches can be broadly categorized into top-down and bottom-up frameworks, each with distinct trade-offs between scalability and precision. However, a convergent limitation across both paradigms is their inadequacy in supporting neighborhood-scale, dynamic decarbonization planning. Top-down methods typically integrate proxy data(e.g., socio-economic indicators, population density, built-form metrics, road networks, and nighttime lights (NTL))with global gridded emission products (e.g., ODIAC, EDGAR, GRACED) and country- or region-specific inventories (e.g., CEADs, CHRED) to downscale emissions to finer spatial units (Cai et al., 2018; Cui et al., 2025; Dou et al., 2022; Zhao & Jiao, 2024; Zheng et al., 2024). While cost-effective for inter-city comparisons, their fundamental reliance on static proxies limits their capacity to capture intra-urban heterogeneity. For instance, NTL is a proxy for lighting activity rather than emissions themselves. It exhibits poor sensitivity to on-road traffic and other diffuse sources, effectively obscuring the very neighborhood-level variations and hourly emission spikes that are critical for local intervention (Gao et al., 2023; Liu et al., 2024b).

In contrast, bottom-up methods compile emissions from fine-scale "point" (e.g., buildings and facilities) and "line" (e.g., roads) sources using detailed spatial datasets. Pioneering projects like Hestia in Indianapolis have demonstrated the feasibility of building- and road-level quantification (Gurney et al., 2012, 2019); subsequent applications across high-density urban areas have utilized dynamic traffic activity, remote sensing, built-environment data, and other spatial information to model and map emissions at high resolution (Chen et al., 2025; Fichera et al., 2016; Guevara et al., 2013; S. Stagakis, Feigenwinter, Vogt & Kalberer, 2023; Wang et al., 2020). Nevertheless, the scalability of such detailed inventories remains a primary constraint, especially in fast-growing cities where infrastructure records are often incomplete (Amjath-Babu et al., 2025; Montfort et al., 2025). A more profound issue is their sectoral isolation; they frequently focus on single sectors and seldom integrate non-traditional sources like human metabolism or the mitigating effect of urban carbon sinks, leading to a fragmented and incomplete urban carbon portrait (Winbourne et al., 2022). Building on this foundation, integrated modeling approaches have emerged that combine multi-source data to quantify cross-sectoral emissions at the neighborhood scale(Luo et al., 2025).

Recently, machine learning (ML) models have emerged as a hybrid pathway, using multi-source data to estimate high-resolution emissions. These approaches demonstrate remarkable versatility, applying diverse data sources to the carbon emission problem. For instance, (Yap et al., 2025) developed a graph deep learning framework that integrates building energy data and multi-modal geospatial inputs to quantify building operating carbon emissions across five cities. Similarly, other efforts have employed computer vision for household emissions while applying natural language processing to map manufacturing sectors (Liu et al., 2025; Wang et al., 2025). Beyond sector-specific studies, ML has also been integrated into spatial simulation: (Luo et al., 2023) combined a BP neural network with land use simulation models to predict the spatial distribution of carbon emissions under different development scenarios.

Despite their predictive power, these data-driven approaches often function as "black boxes," lacking the transparent, process-based mechanisms of traditional inventories. This limits their interpretability and raises concerns about generalizability across cities with different data landscapes and urban forms (Chen & Debnath, 2025). Overall, existing accounting methodologies—spanning top-down, bottom-up, and emerging ML—lack effective cross-sector and cross-scale integration in space and time, constraining their policy relevance at the neighborhood level.

2.2. Sensor technologies for CO_2 measurement and model validation in dense urban areas

The limitations of modeling approaches highlight the critical need for empirical validation. However, a representativeness gap exists between what models can simulate and what available sensors can reliably measure in complex urban settings. Table 1 provides a comparative overview of these sensor technologies. Eddy-covariance (EC) systems provide direct CO_2 flux measurements but are inherently point-based. Their footprint (0.2–5 km^2) is influenced by wind and urban roughness, making them representative of a heterogeneous "source area" rather than a specific neighborhood, and failing to capture the sharp gradients in emission intensity characteristic of dense urban cores (Björkegren & Grimmond, 2018; Christen, 2014; Stagakis et al., 2019).

Mobile sensor platforms mounted on vehicles address the resolution issue, enabling street-level hotspot mapping (Sm et al., 2019). These mobile systems are effective for identifying emission hotspots and

Table 1
Comparative summary of validation sensor technologies for CO_2 measurement.

Technology	Spatial Resolution	Temporal Resolution	Key Strength	Primary Limitation in High-Density Urban Areas
EC system	—	30 min	Direct turbulent CO_2 flux measurement	Limited representativeness and EC-assumption violations in complex urban roughness
Mobile Sensor platform	10–100 m	Seconds	Road-level hotspot mapping	Limited areal coverage; source apportionment ambiguity
LiDAR	120 m	1 min	High temporal and spatial resolution, wide detection range, 3D mapping	High cost; line-of-sight occlusion in dense urban canyons

capturing diurnal patterns when repeated across hours, as reported for high-density neighborhoods in Chinese metropolises (Wu et al., 2025; Zhu et al., 2022). However, their "line-of-sight" coverage is inherently limited, making it challenging to achieve urban–scale coverage without extensive, repeated campaigns. In addition, the challenge of robust source attribution that disentangles the contribution of a specific road from adjacent buildings under complex urban microclimates remains unresolved.

Satellite observations (e.g., OCO-2/3, GOSAT, TANSAT) offer global coverage but face their own set of constraints in urban applications (Hu et al., 2024). Their coarse resolution and high sensitivity to aerosols and clouds often blur the distinct near-surface emission signatures of individual neighborhoods, making them unsuitable for validating models at the block scale (Cui et al., 2025; Y. Wang et al., 2023).

In this context, Light Detection and Ranging (LiDAR) remote sensing, particularly Coherent Differential Absorption LiDAR (CDIAL), presents a transformative opportunity. Scanning CDIAL systems achieve spatial and temporal resolutions of about 120 m and 1 min, and accuracies around ±5 ppm, which bridge the gap between point measurements and coarse satellite data (Koch et al., 2004; Yu et al., 2021, 2024). Crucially, their kilometer-scale detection range and ability to perform 3D mapping provide a spatially representative "snapshot" of the urban CO_2 plume, far exceeding the footprint of an EC tower and the linear path of a mobile platform (Apte & Manchanda, 2024). In urban settings, co-located deployments have enabled simultaneous mapping of CO_2 and wind fields, revealing persistent emission sources in industrial zones and dynamic fluctuations in parks and vegetated corridors (Yue et al., 2022). Despite this potential, the systematic integration of CDIAL measurements as a core validation benchmark for multi-source, neighborhood-scale carbon models remains largely overlooked in current research. Most model validation efforts still rely on sparse ground stations or lack rigorous, high-resolution observational constraints altogether.

In summary, a critical gap remains at the intersection of modeling and validation. While top-down methods lack resolution and bottom-up inventories struggle with scalability and sectoral integration, emerging data-driven approaches often sacrifice interpretability. Concurrently, advances in validation technologies, ranging from eddy covariance and mobile platforms to satellite observations, continue to face fundamental representativeness challenges in the complex, heterogeneous environment of a dense city. While emerging remote sensing techniques like LiDAR/CDIAL offer a promising path forward by providing high-resolution, spatially representative data, their systematic integration as a core validation benchmark for neighborhood-scale, multi-source carbon models remains largely unrealized.

Therefore, there is a pressing need for a unified accounting framework that: (1) achieves the high spatiotemporal resolution of advanced bottom-up and ML methods; (2) provides comprehensive sectoral integration including anthropogenic and ecological processes; and (3) is robustly validated against high-resolution, spatially representative empirical data like that provided by CDIAL. This study aims to address this integrated gap by developing and validating the SCE-Model.

3. Data and methods

3.1. Study area and data sources

3.1.1. Study area

This study focuses on the Old City of Nanjing, China, a historic urban core encircled by Ming Dynasty city walls and a moat system (Fig. 1). The Old City was selected as it presents a representative case of a high-density urban area (25,400 inhabitants per km^2) within a rapidly developing Chinese metropolis. Located in the subtropical monsoon climate zone, Nanjing experiences distinct seasonal demands for both cooling and non-centralized heating, making its emission profile broadly informative for numerous densely populated cities in similar climate regimes across the globe.

In addition, the study area encapsulates the core challenges of dense cities worldwide: intense energy demand, chronic traffic congestion, and intense competition for green space. Critically, it contains a comprehensive suite of urban carbon sources and sinks within its clearly defined historical boundary. This includes a full spectrum of building types, a dense road network, dynamic human populations, and significant blue-green infrastructure. The co-existence of these elements within a single, bound area makes it an ideal natural laboratory to develop our integrated carbon accounting framework. The predominantly flat terrain further minimizes the confounding influence of complex topography on atmospheric dispersion and LiDAR observation, thereby ensuring a clearer attribution of observed CO_2 concentrations to urban activities.

3.1.2. Data sources

This study utilizes two main categories of data: (1) input data for the SCE-Model and (2) LiDAR-based observational data for model validation.

(1) Model input data

To ensure comprehensive and accurate urban carbon emission modeling, we compiled multi-source inputs for the four sub-models from authoritative administrative datasets, remote sensing platforms, open-source repositories, and field surveys. Unless otherwise specified, all data refer to the period from 1 to 30 September 2024 within the Nanjing Old City (local time, UTC+8), ensuring temporal consistency. All datasets were preprocessed to ensure spatial and temporal harmonization, with continuous predictors standardized using Z-scores where applicable. Key data types and sources are summarized in Table 2.

Building upon the multi-source data, the following core indicators were applied for each sub-model to facilitate the spatiotemporal carbon accounting. For building operations sub-model, key inputs included the energy intensity for different end-uses and building types, and fuel-specific emission factor. Then, central to transportation sub-model were the traffic flow and average speed per road segment, coupled with speed-dependent emission factors for various vehicle classes, calibrated using the IVE model. Next, for human metabolic sub-model, the principal component was the hourly dynamic population density, which was converted to emissions using a physiological respiration emission factor. Finally, vegetation carbon sink sub-model's core parameters included the carbon sequestration coefficients for different vegetation types sourced from local greening standards, and the vegetated area coupled with NDVI values. These parameters serve as the direct inputs to the mathematical formulations detailed in Section 3.4.

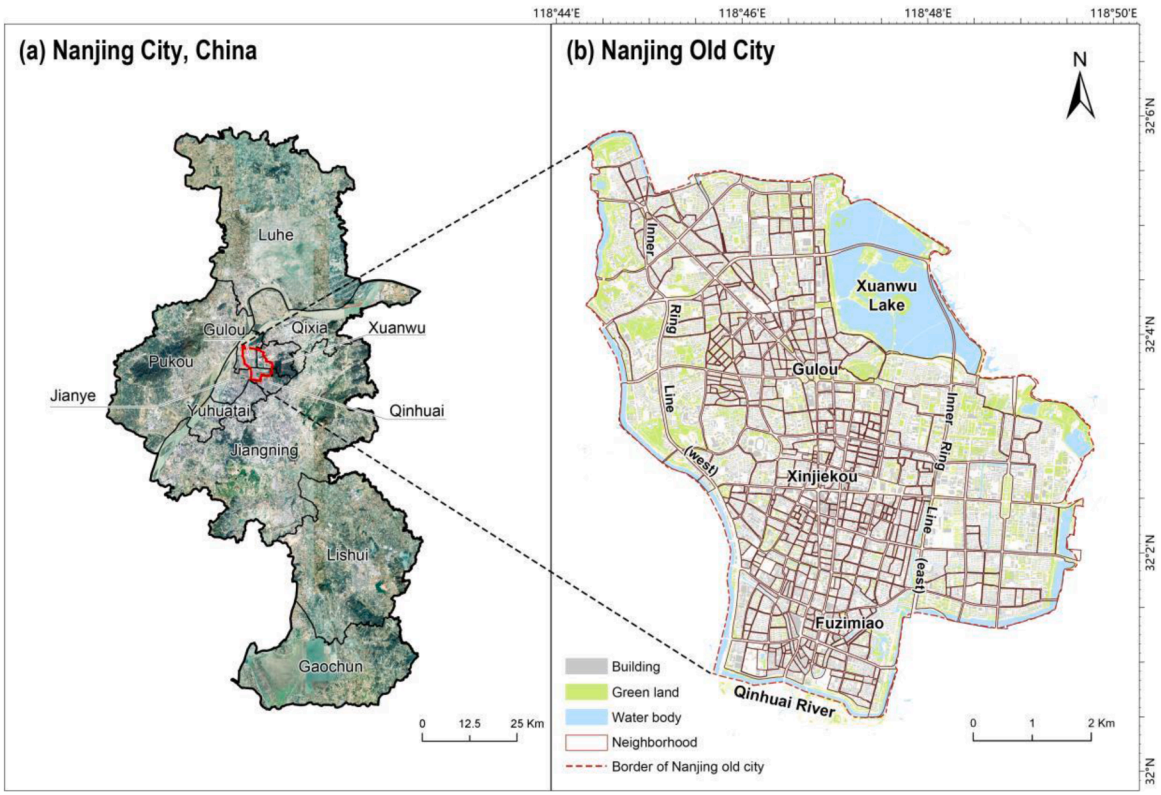

Fig. 1. Map of the study area: (a) Location of the Old City within Nanjing; (b) Detailed view of the Old City, bounded by the ancient city wall, showing major landmarks and the distribution of neighborhoods, buildings, green spaces, and water bodies.

Table 2
Overview of model input data and sources.

Sub-Model	Data Type	Temporal Resolution	Spatial Resolution	Source	Role in Methodology
Building operations	Building energy data	Hourly	Building-level	Building energy simulation; field gas consumption surveys	To calculate the hourly building energy emission intensity
	3D building data	Static (year 2024)	Building-level	OpenStreetMap (OSM); real estate platforms	To extract building footprint area and attributes for energy modeling
	AOI data	Static (year 2024)	Area-of-Interest	Amap API	To identify building functions for assigning activity profiles
	Meteorological data	hourly	City-wide	EnergyPlus typical meteorological year (TMY)	Driving data for building energy simulation
Transportation	Traffic status data	Hourly	Road segment	Amap API	To estimate hourly traffic volume and congestion levels
	Urban road network data	Static (year 2024)	Road segment	OpenStreetMap (OSM)	To define road segment geometry (length, type)
	Vehicle fleet composition	Annual (year 2023)	City-level	Municipal traffic statistics yearbook	To determine the proportion of vehicle types for emission factors
Human metabolic	Resident population	Annual (census year)	District-level	District census data	To estimate baseline population distribution
	Dynamic population density	Hourly	120 m grid	Baidu heatmap API	To downscale the population to an hourly resolution
Vegetation carbon sink	Carbon sequestration coefficients	Annual	Species-level	Local greening standards	To assign sequestration rates by vegetation type
	Vegetation indices (NDVI)	Monthly (year 2024)	10 m grid	Sentinel-2 via Google Earth Engine	To map the spatial extent and phenological dynamics of green spaces

(2) CO_2 observational data

During the field campaign, near-surface CO_2 concentration and wind field measurements were obtained using a CDIAL system. The campaign was conducted from 17 to 19 September 2024 atop a 50-meter building on the Southeast University campus (see Fig. 2).

Table 3 summarizes the key operational parameters used during the campaign. All model inputs and remote sensing observation data streams were spatiotemporally harmonized to enable direct comparative analysis. Detailed data processing and quality control procedures are described in Supplementary material S1.

3.2. *Framework of the SCE-Model*

This study develops a high-resolution, dynamic carbon-emission modeling framework to identify emission hotspots and propose targeted mitigation strategies in high-density urban areas. Operating at neighborhood-scale spatial and hourly temporal resolution, the SCE

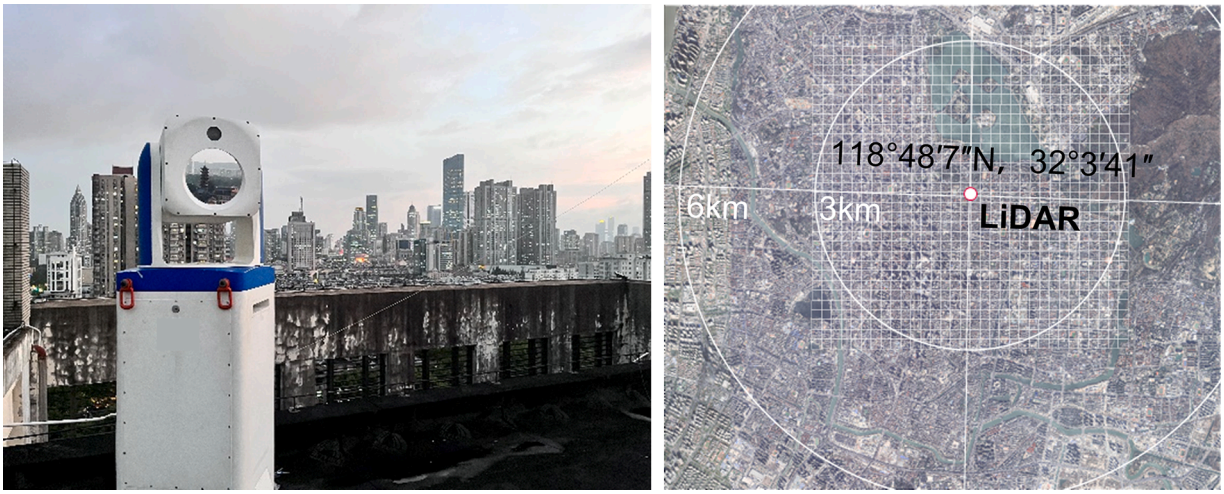

Fig. 2. Photograph of the observation site during the campaign, illustrating the LiDAR installation and its surrounding coverage.

Table 3
CDIAL system operational parameters during the campaign.

Parameter	Value	Unit
Maximum measurement range	6	km
Spatial resolution	120	m
Temporal resolution	1	min
Wavelength	1572	nm
Measurement accuracy (CO_2)	±5	ppm

model is validated against near-surface CDIAL CO_2 measurements to assess and improve accuracy. The framework offers comprehensive urban carbon accounting and mapping by integrating four sub-models: building operations, transportation, human metabolism, and vegetation carbon sinks.

To address the challenges of complex spatiotemporal carbon monitoring, the framework comprises four core steps (Fig. 3):

(1) Multi-source data integration: Integrate heterogeneous multi-source urban datasets (e.g., 3D building data, traffic status data, population heatmap data, and remote sensing).
(2) Urban carbon modeling: Implement the four sub-models, combining machine-learning methods with physics-based emission models to capture nonlinear interactions.
(3) LiDAR-enabled model validation: Employ near-surface CDIAL CO_2 observations for high-resolution model validation.
(4) Strategy formulation: Apply clustering analysis to identify emission typologies and inform neighborhood-specific decarbonization strategies.

3.3. Scope and system boundary

This study focuses on direct carbon emissions (Scope 1) originating from on-site human activities in high-density urban environments, specifically covering the residential, commercial, and transportation sectors (see Fig. 4). Scope 1 emissions are prioritized as they are directly related to local activities and can be effectively influenced by urban planning interventions.

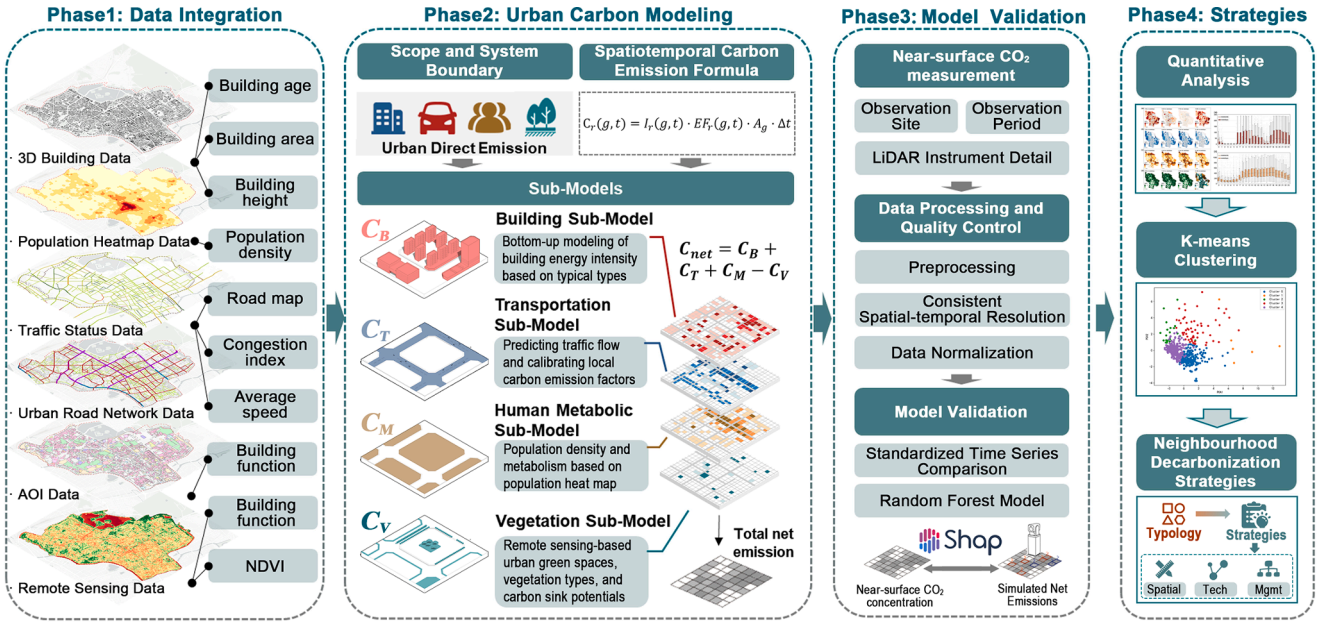

Fig. 3. The design framework of the SCE-Model.

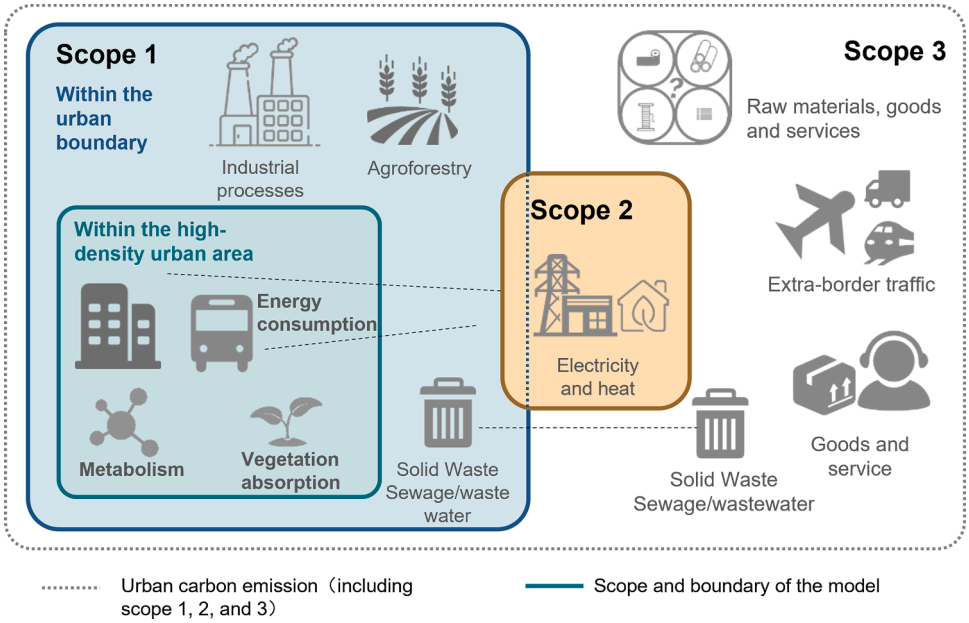

Fig. 4. Scope and system boundary. This diagram defines the scope and system boundary of carbon accounting for this study. Although Scope 1 (direct), Scope 2 (indirect, imported energy), and Scope 3 (supply chain) emissions are all illustrated for completeness, our analysis is exclusively focused on Scope 1 emissions and sinks within dense urban areas. In this context, transportation, building operations, and human metabolism are carbon sources, while vegetation absorption is the only carbon sink. Scope 2 and Scope 3 emissions are excluded from the quantitative analysis.

The system boundary encompasses four primary sources: (1) building operations, primarily from fossil fuel combustion (e.g., natural gas, LPG, coal); (2) transportation, covering tailpipe emissions of gasoline and diesel vehicles; (3) human metabolism, referring to CO_2 generated from population respiration; and (4) urban carbon sinks, including vegetation photosynthesis and carbon sequestration. Such a sub-model decomposition has been widely adopted in recent urban carbon emissions modeling studies and inventories, enabling methodological consistency and cross-city comparability (Christen et al., 2011; Järvi et al., 2019; Kellett et al., 2013; S. Stagakis, Feigenwinter, Vogt & Kalberer, 2023; Velasco, 2021; Wang et al., 2020; Ye et al., 2023).

3.4. Spatiotemporal carbon emission formula and sub-models

3.4.1. Spatiotemporal carbon emission formula

Tiered inventory methods rooted in the IPCC framework often lack explicit spatiotemporal dynamics unless tightly coupled with activity data and process models. To address this, we formulate emissions (or sinks) on sectors, discrete spatial units, and time steps:

$$C_r(g,t) = I_r(g,t)\cdot EF_r(g,t)\cdot A_g\cdot \Delta t \quad (1)$$

Where $r \in \{B,\ T,\ M,\ V\}$ denotes emission sectors: building operations(B), transportation(T), human metabolism(M), and vegetation carbon sinks(V); g is a spatial unit(block) with area $A_g(m^2)$; t indexes time steps of duration $\Delta t(h)$; $I_r(g,t)$ is the activity intensity for sector r; $EF_r(g,t)$ is the corresponding emission/sink factor consistent with I_r. This formulation makes local variability explicit and is scalable across urban extents and temporal resolutions.

The net carbon flux for each spatial unit g at time t are:

$$C_{net}(g,t) = C_B(g,t) + C_T(g,t) + C_M(g,t) - C_V(g,t) \quad (2)$$

By convention, $C_V(g,t)$is defined as a positive uptake. This framework supports hotspot mapping and policy design at neighborhood to city scales.

3.4.2. Building operations mission sub-model

This sub-model quantifies direct CO_2 emissions from fossil fuel combustion (natural gas, LPG, coal) for space heating, cooking, and domestic hot water:

$$C_B(g,t) = \sum_{i\in g}\sum_j I_{i,j}(t)\cdot A_i\cdot EF_{i,j} \quad (3)$$

Where i denotes buildings located within block g; A_i is floor area (m^2); j denotes end-use activity; $I_{i,j}(t)$ is energy intensity ($MJ\cdot m^{-2}\cdot h^{-1}$); and $EF_{i,j}$ is the emission factor ($kg\ CO_2\cdot MJ^{-1}$). This formulation enables block-level differentiation by building type, function, and temporal patterns. Alternative fuel-based form (equivalent when data permit):

$$C_B(g,t) = \sum_{i\in g}\sum_j \left[Q_{i,f}(t)\cdot EF_f\right] \quad (4)$$

Where $Q_{i,f}(t)$ is fuel consumption rate ($MJ\cdot h^{-1}$); EF_f is the fuel-specific factor.

3.4.3. Transportation emission sub-model

This sub-model quantifies direct CO_2 emissions from urban fossil-fuel vehicles (private cars, buses, taxis, freight trucks). Key parameters include road type, spatiotemporal traffic flow, vehicle fleet composition, and speed-dependent emission factors. Traffic flow is estimated using a hybrid approach integrating a physical traffic-flow model with residual correction via machine learning to capture rush hours and congestion:

$$E_Z(t) = \sum_k \left[F_{z,k}(t)\cdot L_z\cdot e_k\left(v_{z,k}(t)\right)\right] \quad (5)$$

$$C_T(g,\ t) = \sum_{z\in Z_g}\left[\frac{E_z(t)}{n_g(z)}\right] \quad (6)$$

Where z indexes road segments; Z_g denotes segments associated with block g; $n_g(z)$ is number of blocks adjacent to segment z; L_z is segment length(km); k indexes vehicle classes; $F_{z,k}(t) = F_z(t)\cdot P_{z,k}(t)$ is hourly flow of class k ($veh\cdot h^{-1}$), from total flow $F_z(t)$ and class share $P_{z,k}(t)$; $v_{z,k}(t)$ is average speed ($km\cdot h^{-1}$); and $e_k(\cdot)$ is the speed-dependent emission factor ($kg\ CO_2\cdot(veh\cdot km)^{-1}$); factors e_k are calibrated using the IVE model and local measurements.

3.4.4. Human metabolic emission sub-model

Human respiration contributes a direct, measurable CO_2 source that, while modest citywide, can be non-negligible in high-density settings. At

the neighborhood scale, emissions are computed per block and aggregated:

$$C_M(g,t) = \rho M(g,t) \cdot A_g \cdot EF_M \tag{7}$$

$$C_M(t) = \sum_g C_M(g,t) \tag{8}$$

Where$M(g,t)$ is population density (persons·m^{-2}); A_g is block area (m^2); and EF_M is the respiration emission factor (kg CO$_2$·person^{-1}·h^{-1}), set to 0.042 kg CO$_2$·person^{-1}·h^{-1} based on physiological studies (Moriwaki & Kanda, 2004; S. Stagakis, Feigenwinter, Vogt, Brunner et al., 2023; Ueyama & Takano, 2022). Hourly population fields are derived using census data with high-resolution population heatmaps (120 m), followed by spatiotemporal interpolation and normalization.

3.4.5. Vegetation carbon sink sub-model

Urban vegetation is a primary CO$_2$ sink via photosynthesis and soil carbon sequestration. Using the Normalized Difference Vegetation Index (NDVI) from high-resolution remote sensing imagery, vegetation is classified into trees, shrubs, and grassland. Block-level annual sequestration is computed as:

$$C_V(g, annual) = \sum_q \left[\sigma_q \cdot \mathrm{A}_{q \in g}\right] \tag{9}$$

$$C_V(g,\ t) = \left[\frac{C_V(g, annual) \cdot NDVI_{g,m(t)}}{\sum_{j=1}^{12} NDVI_{g,j} \cdot N_{m(t)}}\right] \cdot \frac{\phi_{m(t)}(\mathrm{h})}{H_m} \tag{10}$$

Where q denotes vegetation class; σ_q is net annual sequestration coefficient (kg CO$_2$·m^{-2}·yr^{-1}); A$_q$ is the area of vegetation class q within block g (m^2); $NDVI_{g,m}$ is monthly NDVI value for block g, N_m is number of days in month m; $\phi_{m(t)}$ is diurnal photosynthetic weight, and H_m is daily normalization constant.

Methodological details are provided in Supplementary material S2, which presents workflow diagrams and key parameters for the four sub-models.

3.5. Validation method using ground-based lidar remote sensing

To validate the spatiotemporal accuracy of the SCE model, a ground-based LiDAR remote sensing campaign was conducted using the CDIAL system. This instrument simultaneously measures path-integrated CO$_2$ mixing ratios and wind vectors via the optical Doppler effect, constructing 2D spatial maps through Plan Position Indicator (PPI) scanning.

Calibrated, quality-controlled CO$_2$ retrievals, validated against a cavity ring-down spectrometer ($R^2 > 0.9$, RMSE < 6 ppm) (Yu et al., 2024), served as the independent benchmark. Model outputs were evaluated using two methods: (1) spatiotemporal pattern correlation analysis, which quantitatively evaluated the agreement between standardized and background-corrected model outputs and observations after temporal aggregation and spatial matching; and (2) a machine learning-based inversion approach employing a Random Forest (RF) regression model. The RF model incorporated simulated net emissions, key meteorological variables, and temporal predictors as input features to predict the observed CO$_2$ mole fractions.

Model performance was quantified using the coefficient of determination (R^2), mean squared error (MSE), and mean absolute error (MAE). A Shapley Additive exPlanations (SHAP) analysis was applied to the RF model to interpret the influence of the predictive factors.

3.6. Typology of urban carbon emission neighborhoods

The K-means clustering algorithm was applied to neighborhood-level emission data to identify neighborhoods with similar carbon emission characteristics. All variables were standardized using Z-score normalization. The optimal number of clusters ($k = 5$) was determined by the Elbow Method to balance interpretability and clustering accuracy. The input variables (Table 4) capture multidimensional emission dynamics, including sectoral emissions, proportional structure, carbon sink capacity, and spatial intensity. Mathematical formulations and clustering parameters are provided in Supplementary material S3.

4. Results

4.1. Quantitative analysis of direct carbon emissions

4.1.1. Sectoral and daily patterns of carbon emissions

This section presents a quantitative analysis of direct carbon emissions across the four sectors at a daily resolution. The analysis elucidates the magnitude and spatial distribution patterns, establishing a foundational understanding of the aggregate carbon budget within the study area.

Quantitative analysis revealed stark sectoral disparities in carbon emissions across Nanjing Old City (Figs. 5–8). Building operational emissions averaged 0.84 million kg CO$_2$/day during the study period. Fig. 5 presents the spatial distribution of building emissions, with peripheral neighborhoods dominating absolute emissions due to larger built-up footprints. At the same time, high-density mixed-use zones in the urban core showed the highest per-unit-area emission intensity. Analysis of end-use contributions revealed that domestic hot water accounted for the majority (71.5 %) of building emissions, with cooking constituting the remainder (Fig. 5c). By building function, residential structures were the primary contributor (81.3 %), significantly surpassing emissions from commercial and public buildings (Fig. 5d). Notably, among residential types, buildings with ground-floor catering uses emitted 1.2 times higher than those of purely residential buildings. Validation against municipal statistics on residential natural gas and LPG consumption confirmed reliability, with a deviation of 9.1 %.

Transportation emissions remained relatively stable at approximately 1.05 million kg CO$_2$/day (Fig. 6). While expressways and major roads exhibited higher per-segment emissions due to concentrated traffic flows along key corridors, side streets collectively dominated the sector-wide emissions, contributing 38.7 % of the daily total. This pattern reflects their extensive network density and persistently high

Table 4
Variables for neighborhood carbon emission typology.

Type	Indicator	Symbol	Description
Emission indicators	Building emissions	C_B	Daily carbon emissions from building operations (kg CO$_2$/day)
	Transportation emissions	C_T	Daily carbon emissions from transportation (kg CO$_2$/day)
	Human metabolism emissions	C_M	Daily carbon emissions from human metabolic activity (kg CO$_2$/day)
	Net total emissions	C_{net}	Net total carbon emissions (kg CO$_2$/day)
Proportional indicators	Building emission share	S_B	Proportion of building emissions (%)
	Transportation emission share	S_T	Proportion of transportation emissions (%)
Carbon sink attributes	Vegetation carbon sequestration	C_V	Daily carbon sequestration by vegetation (kg CO$_2$/day)
	Vegetation mitigation share	S_V	Proportion of emissions offset by vegetation (%)
Spatial intensity indicator	Net emission intensity	E_{net}	Net carbon emissions per unit area (kg CO$_2$/m^2/day)

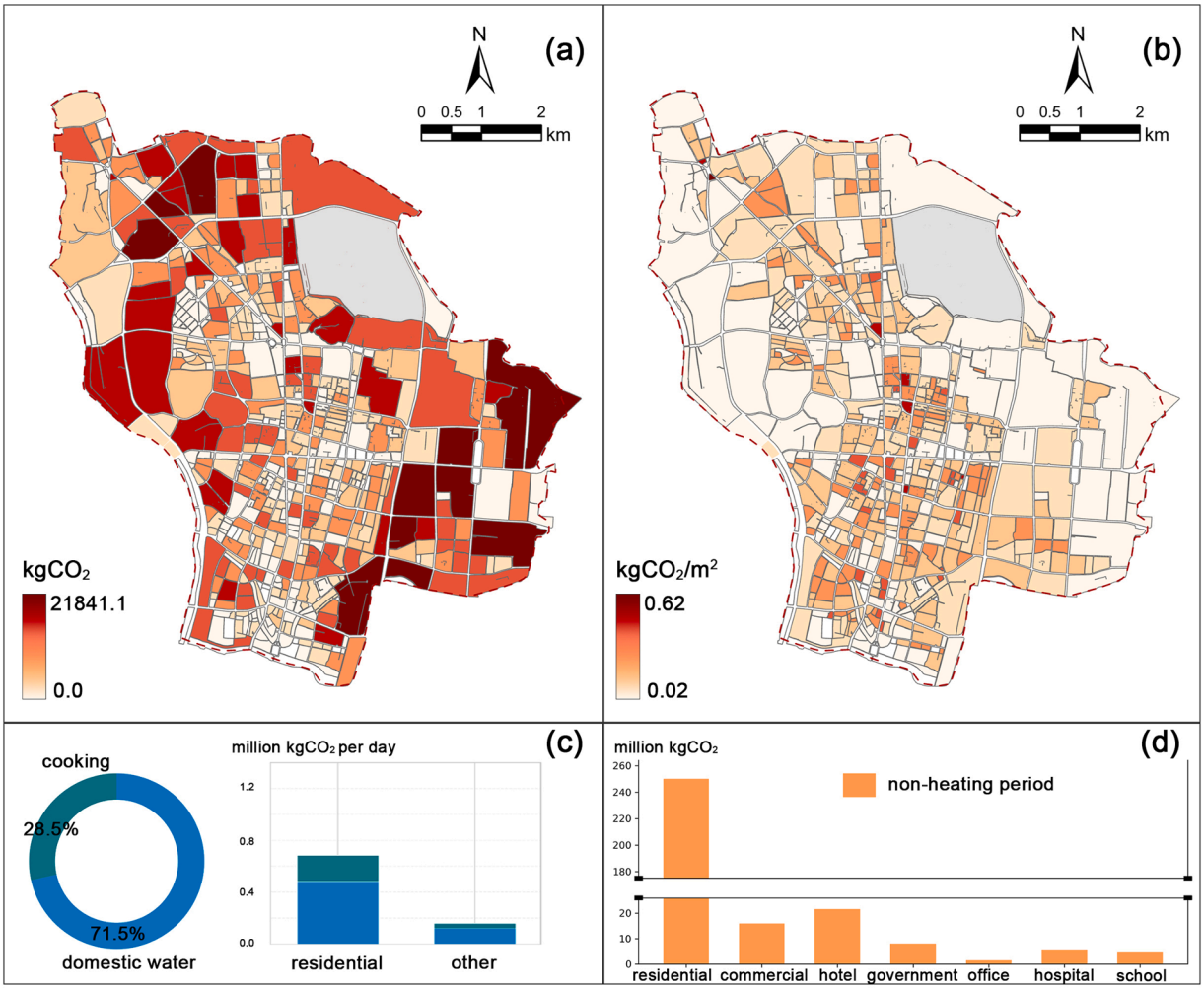

Fig. 5. Modeled building operation emissions. (a) Spatial distribution of daily total building emissions (kg CO_2/ day), (b) Spatial distribution of emission intensity (kg CO_2/m^2/day), (c) Fractional contributions of end-use activities to daily emissions (cooking, domestic hot water), (d) Daily emissions by building function (million kg CO_2/day).

volumes of short-distance trips in high-density urban areas. Major roads (23.3 %) and secondary roads (20.8 %) were significant secondary sources, with emissions spatially concentrated around transportation hubs.

Human metabolic emissions emerged as the dominant source, averaging 6.17 million kg CO_2/day (±6.62 % daily variation), significantly exceeding emissions from other sectors. This establishes a critical baseline range for urban metabolic footprint assessment. Fig. 7a shows a pronounced multicore, clustered pattern anchored by major commercial and functional agglomerations. The Xinjiekou core formed the most significant emission hotspot, with the peak neighborhood reaching 0.03 million kg CO_2/day; the broader Xinjiekou cluster accounted for 27.3 % of the Old City's total metabolic emissions, extending north–south and exhibiting a belt-like morphology. By functional category, hospital-dominated neighborhoods accounted for the largest share of metabolic emissions, followed by commercial and residential areas (Fig. 7c). In contrast, hotel-dominated neighborhoods exhibited the highest per-unit-area emission intensity (Fig. 7d).

In contrast, urban green spaces provided only a modest carbon sink, with a mean sequestration of 0.04 million kg CO_2/day, offsetting approximately 0.6–0.7 % of anthropogenic emissions in Nanjing Old City. Substantial spatial heterogeneity was observed: green spaces within commercial, governmental, and office districts exhibited the highest uptake, whereas hospital-, hotel-, and school-dominated areas showed lower sequestration; residential neighborhoods were highly variable but displayed a notably low median uptake (Fig. 8d). This pattern indicates an inequitable distribution of carbon-sequestration assets, with pronounced deficits in emission-intensive residential zones.

4.1.2. *Hourly and spatiotemporal dynamics of emissions*

Building upon the daily analysis, this section delves into the spatiotemporal dynamics of emissions at an hourly resolution. It aims to unravel each sector's distinct diurnal fluctuation patterns and synergistic effects, collectively shaping the temporal evolution and spatial migration of emission hotspots throughout the day.

Integrated spatiotemporal analyses reveal that emission rhythms and spatial configurations collectively shape neighborhood-scale carbon footprints (Figs. 9–10). Building operations exhibited pronounced spatiotemporal coupling. On weekdays, emissions followed a double-peaked (M-shaped) diurnal profile, with peaks at 06:00–09:00 and 18:00–20:00 and troughs around 02:00–05:00 and 15:00–16:00; on weekends, peaks attenuated and shifted later (Fig. 9a). Spatially, morning/evening peaks were strongest in peripheral residential belts 2–5 km from the central business district (CBD). In contrast, midday emissions shifted into the urban core, concentrating around Xinjiekou and Gulou (Fig. 10a).

Transportation emissions were tightly commute-synchronized. Temporally, a robust double-peaked diurnal profile coincided with weekday rush hours (07:00–09:00; 17:00–19:00), with weekend totals declining by 18–22 % (Fig. 9b). Spatially, hotspots anchored along

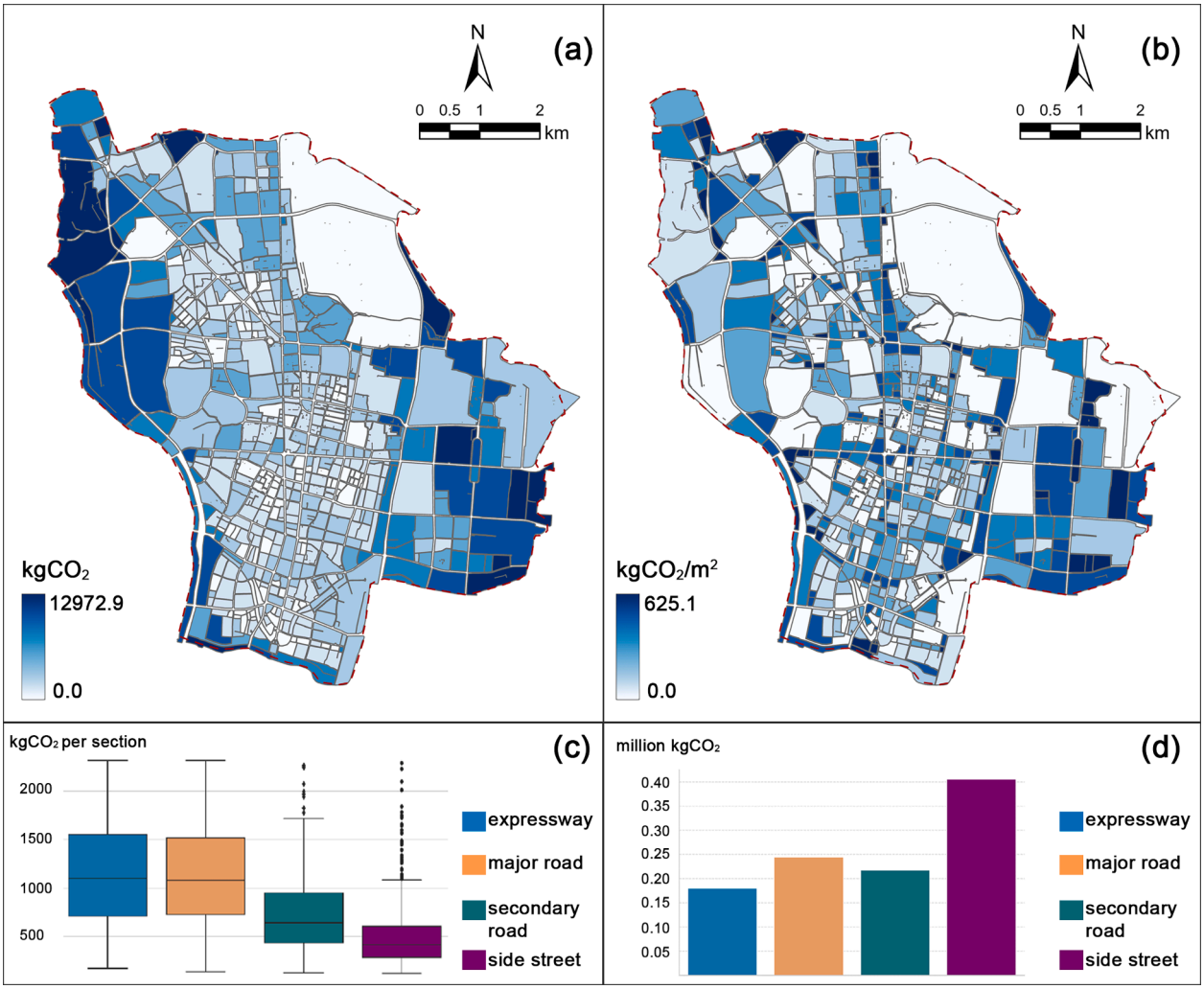

Fig. 6. Modeled transportation emissions. (a) Spatial distribution of daily total emissions (kg CO_2/day), (b) Spatial distribution of emission intensity (kg CO_2/m^2/day), (c) Per-segment emission magnitude by road type (kg CO_2/segment), (d) Aggregate daily emissions by road type (million kg CO_2/day).

expressway corridors, major intersections, and transportation hubs and persisted throughout the day, reflecting network constraints (Fig. 10b). In the Old City, intersections along the inner ring roads, as well as the southeastern gateway where the Shanghai–Nanjing Expressway enters the city, sustained all-day concentrations, underscoring network lock-in.

Human metabolic emissions closely tracked population activity. They exhibited a smooth, wave-like diurnal cycle with a sustained daytime plateau from late morning to early evening (11:00–18:00), coinciding with maxima in commercial and outdoor activities (Fig. 9c). Hotspots migrated diurnally along the core–corridor system: during peak-activity periods, emissions concentrated in the Xinjiekou and Fuzimiao cores and along adjoining arterial commercial corridors; during off-peak periods, core intensities declined and outward spread was limited (Fig. 10c). Despite this migration, high-emission blocks showed pronounced persistence: the Xinjiekou core functioned as an all-day anchor, with peak-hour metabolic emissions within the district exceeding 1.5×10^3 kg CO_2 h^{-1}, evidencing the combined effect of commercial intensity and human presence.

Vegetation carbon sinks operate at counterpoints to anthropogenic fluxes. Temporally, the vegetation sink showed a single-peak noon maximum during peak photosynthesis and shifted to a slight net biogenic release at night due to plant respiration (Fig. 9d). Spatially, sink capacity was significantly inequitable: it concentrated in expansive green infrastructure (e.g., Xuanwu Lake Park, Qinhuai River Greenways), whereas central and southern high-density residential districts exhibited minimal offset capability—often below 5 % of park sequestration (Fig. 10d).

4.1.3. *Neighborhood emission typologies*

Building on the previously derived spatiotemporal emission profiles, we applied k-means clustering to categorize the 546 neighborhoods of Nanjing Old City into five distinct carbon emission typologies (Fig. 11): low-emission, building-dominated, mixed high-emission, transportation-dominated, and high carbon-sink neighborhoods.

Low-emission neighborhoods constitute approximately 45.0 % of neighborhoods. This typology is defined by low emissions across all categories—including building emissions (252.6 kg CO_2/day), transportation emissions (1258.1 kg CO_2/day), and total net emissions (1510.7 kg CO_2/day)—and exhibits a moderate emission intensity (0.078 kg CO_2/m^2/day). Geographically, they cluster in low-density residential and institutional zones (Fig. 11a).

Building-Dominated Neighborhoods accounted for 38.5 % of neighborhoods. Characterized by high building emissions (1377.1 kg CO_2/day) that contribute 55.3 % of their total, these areas exhibit moderate net emissions (2478.6 kg CO_2/day) but low spatial intensity (0.059 kg CO_2/m^2/day), typical of residential-commercial mixed-use districts (Fig. 11b).

Mixed High-Emission Neighborhoods (10.8 % of total) are hotspots where high building (2085.2 kg CO_2/day) and exceptionally high

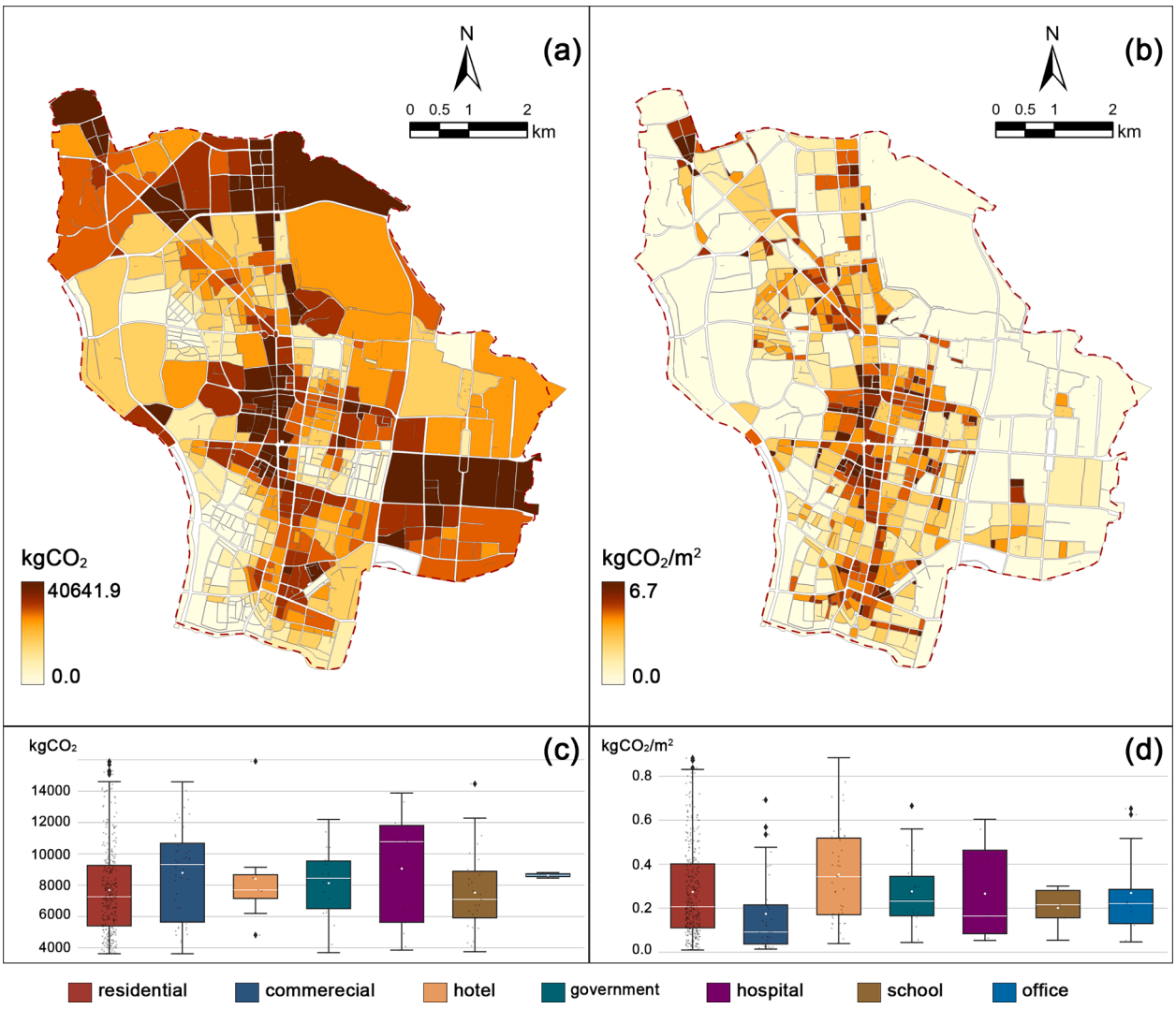

Fig. 7. Modeled human metabolic emissions. (a) Spatial distribution of daily total emissions (kg CO_2/day), (b) Spatial distribution of emission intensity (kg CO_2/m^2/day), (c) Daily emissions by neighborhood primary function (kg CO_2/day), (d) Emission intensity by neighborhood primary function (kg CO_2/m^2/day).

transportation emissions (4857.1 kg CO_2/day) converge with minimal sink capacity. Transportation dominates (71 % of anthropogenic emissions), driving their net emissions to the highest observed (6942.3 kg CO_2/day). They are primarily located along primary arterial roads and commercial and public service zones (Fig. 11c).

Transportation-Dominated Neighborhoods, though rare (4.6 %), are the most intense per-unit-area emitters (0.397 kg CO_2/m^2/day)—1.38 times higher than that of Mixed High-Emission Neighborhoods. Emissions in these zones are overwhelmingly from transportation (89.6 %), pinpointing critical infrastructure bottlenecks like major highways and interchanges as supreme urban carbon hotspots (Fig. 11d).

High Carbon-Sink Neighborhoods are the rarest (1.1 %) but ecologically vital. Comprising parks and natural landscapes, they act as net carbon sinks (−95.8 kg CO_2/day), offsetting 26.4 % of their theoretical emissions and providing a crucial ecosystem service to the broader urban area (Fig. 11e).

4.2. *LiDAR-enabled high-resolution model validation*

Fig. 12a maps the near-surface CO_2 concentrations in four azimuthal sectors surrounding the CDIAL observation site. For validation, we compared standardized simulated net emissions (SNE) against the CDIAL-derived observations (CO_2) across multiple hours and urban blocks. Both time series were standardized to a mean of zero and a standard deviation of one (z-score) over the analysis period to enable direct comparison of their temporal dynamics.

The standardized time series exhibited close agreement (Fig. 12b), with observed concentrations closely tracking the simulated emissions, particularly at night, in the early morning, and in the afternoon. Notably, over 68 % of the CDIAL observations fell within the ±1 standard deviation envelope of the simulated series, providing strong statistical support for the model's reliability at the neighborhood scale.

To further quantify the relationship, a random forest (RF) model was trained using SNE and meteorological covariates to predict the observed CO_2 at the block–hour scale. The model demonstrated strong predictive power (R^2 = 0.79; n = 821) with low error rates (MAE = 7.38 ppm; RMSE = 10.35 ppm). SHAP analysis (Fig. 13) identified SNE as the dominant predictor of observed concentrations, with wind speed and observation height also being significant contributing factors.

It is important to note that while CDIAL provides high-precision concentration measurements, validation in dense urban settings remains challenging due to complexities in vertical mixing and boundary-layer dynamics (Gurney et al., 2021; Lian et al., 2023; Mueller et al., 2021), which can introduce uncertainty. Our SHAP analysis (Fig. 13) provides contextual insight into these effects, indicating that meteorological factors proxying for vertical mixing (e.g., wind speed) were

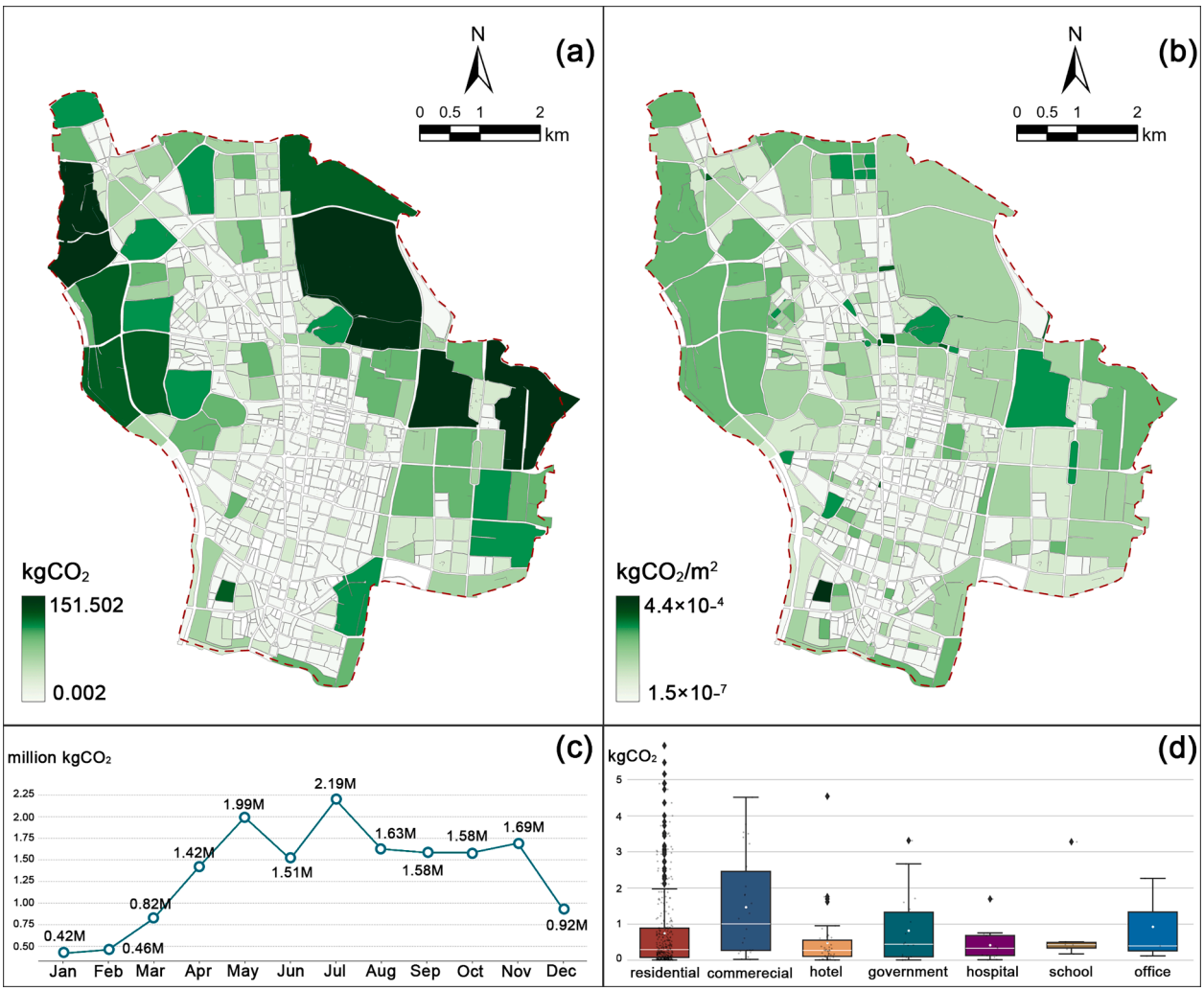

Fig. 8. Modeled vegetation carbon sinks. (a) Spatial distribution of daily total sinks (kg CO_2/day), (b) Spatial distribution of sink intensity (kg CO_2/m^2/day), (c) Urban vegetation carbon sinks for 12 months (million kg CO_2/annual), (d) Daily carbon sequestration by neighborhood primary function (kg CO_2/day).

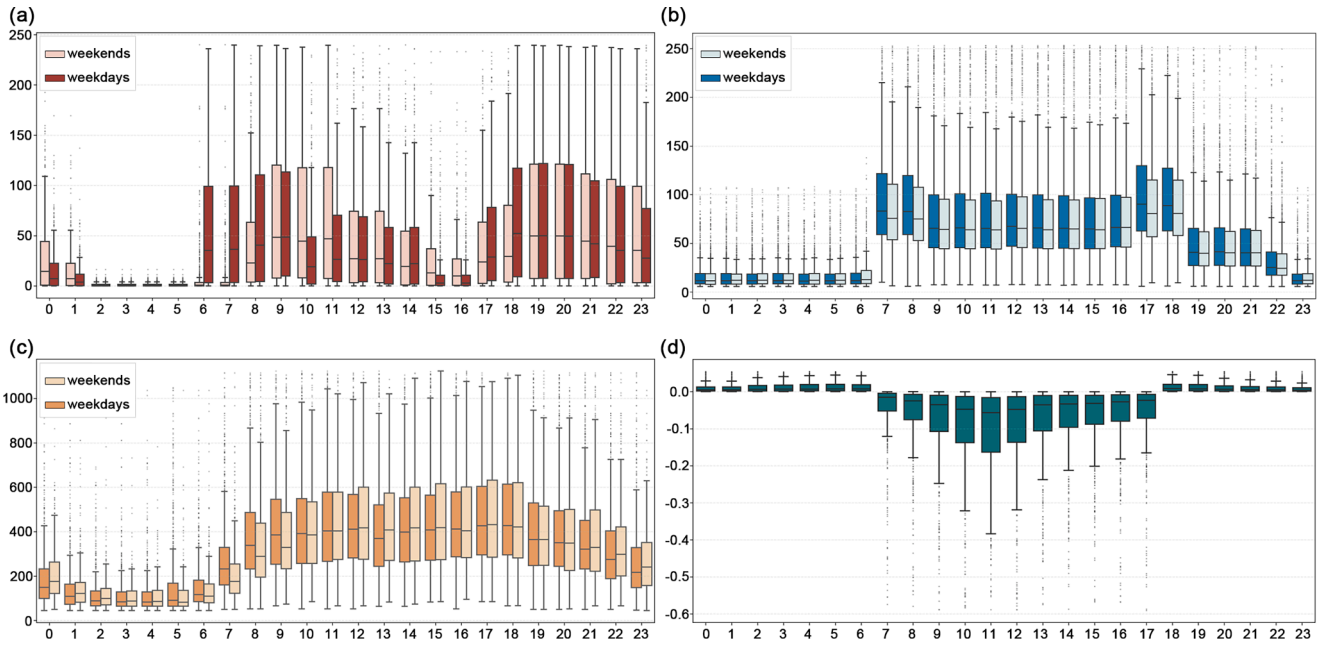

Fig. 9. Diurnal profiles by source (weekday and weekend). (a) Building operations, (b) Transportation, (c) Human metabolism, (d) Vegetation carbon sink.

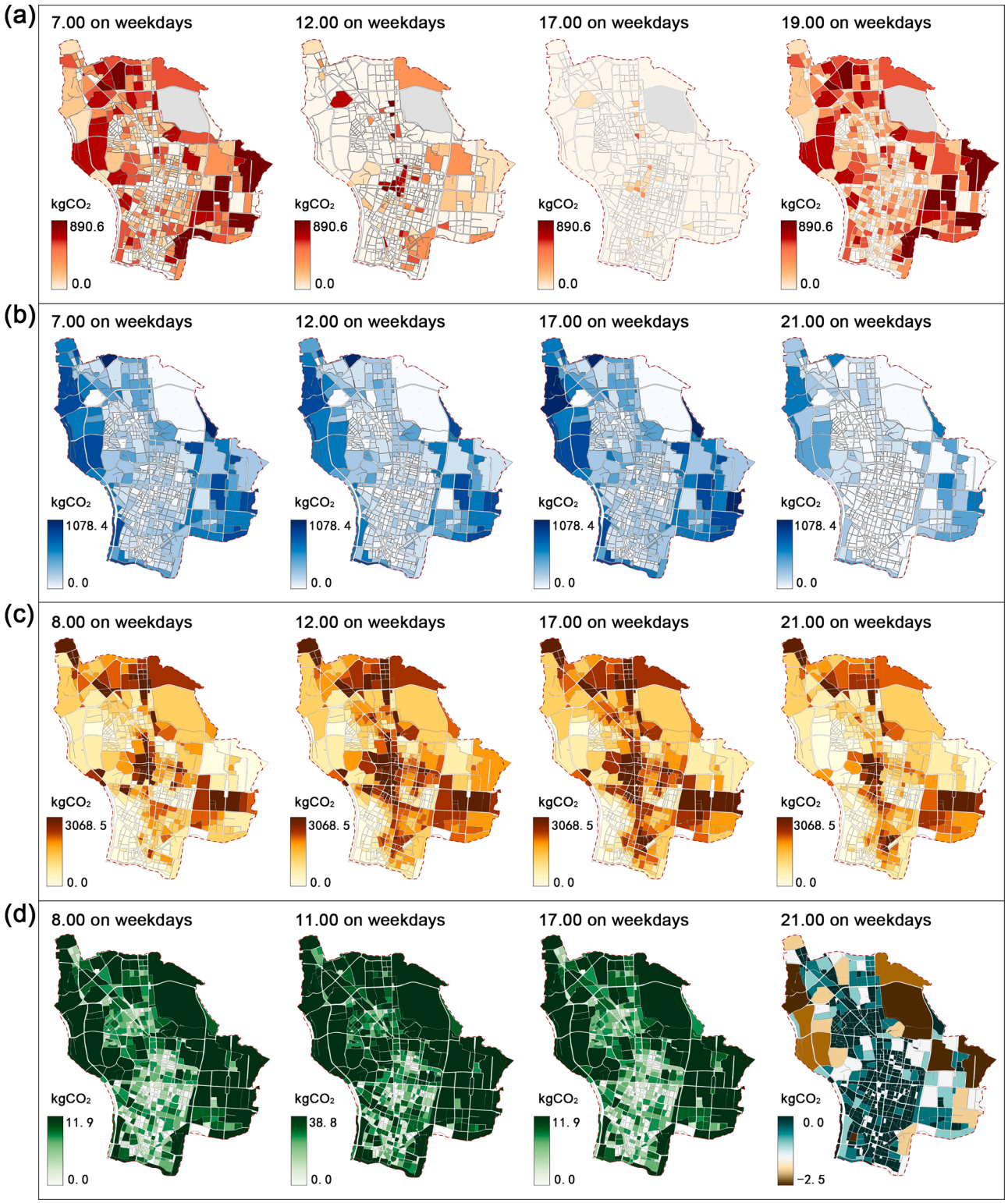

Fig. 10. Weekday spatial dynamics by source/sink. (a) Building operations, (b) Transportation, (c) Human metabolism, (d) Vegetation carbon sink.

secondary factors in influence in addition to the simulated emissions themselves. Despite these challenges, the SCE-Model's high predictive accuracy, consistent temporal patterns, and interpretable driver hierarchy indicate its robustness in capturing neighborhood-scale carbon emission dynamics.

5. Discussion

5.1. Spatiotemporal patterns of carbon emissions in high-density urban areas

Quantitative results from the SCE-Model reveal pronounced spatiotemporal heterogeneity in carbon emissions across Nanjing Old City. A key finding is the dominance of human metabolic CO_2, contributing 76.6

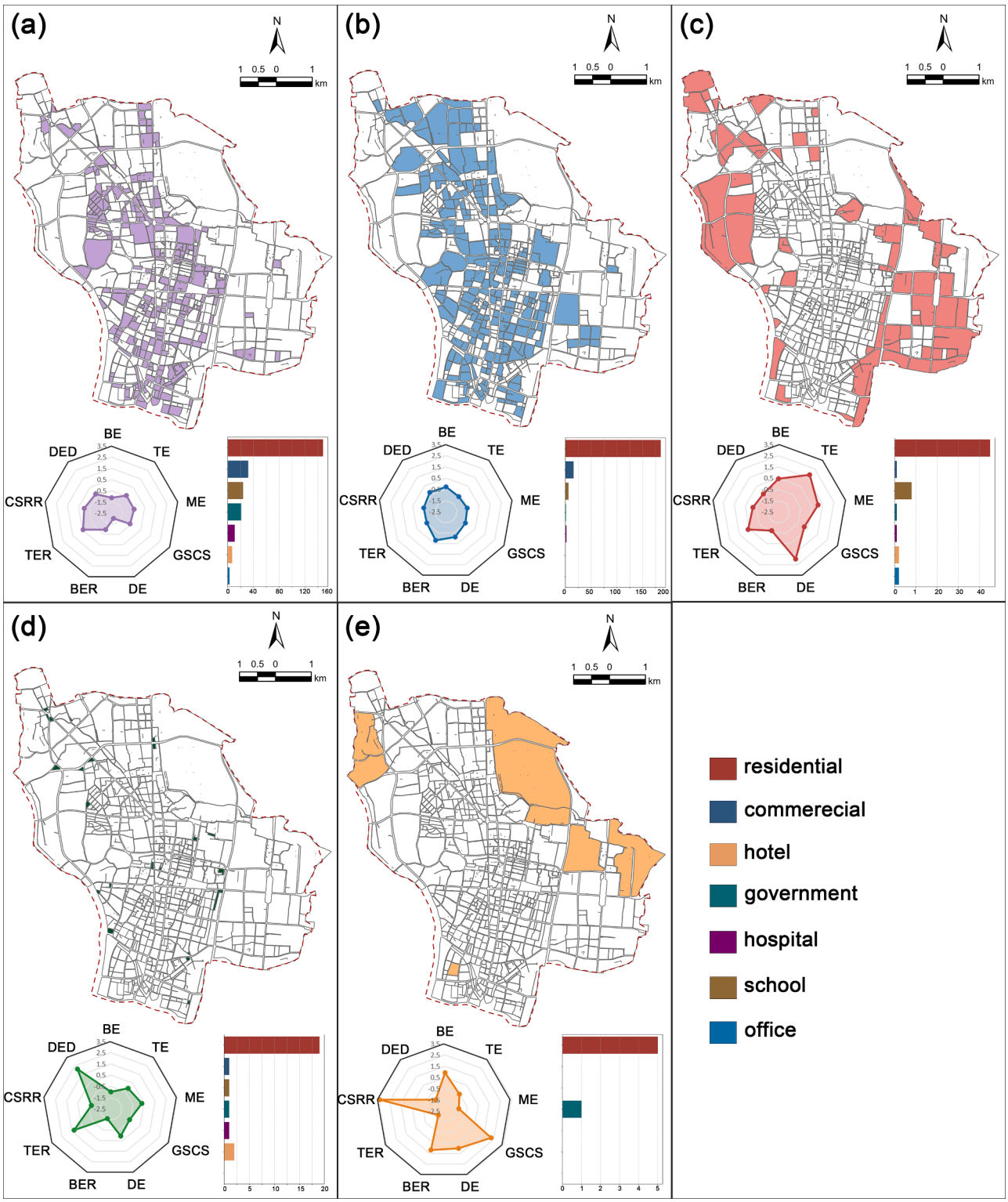

Fig. 11. Spatial distribution and characteristic radar plots of the five neighborhood carbon emission typologies derived from k-means clustering: (a) Low-emission, (b) Building-dominated, (c) Mixed high-emission, (d) Transportation-dominated, (e) High carbon-sink.

% of total anthropogenic emissions—significantly higher than levels reported in Vancouver (8 %; Christen et al., 2011; Kellett et al., 2013), central London (14 %; Björkegren & Grimmond, 2018), and Toulouse (10 %; Goret et al., 2019), where building energy and transport typically dominate. This aligns more closely with estimates from Tokyo (38 %; Moriwaki & Kanda, 2004) and Helsinki city center (39 %; Järvi et al., 2019). Several factors explain this disparity: firstly, Nanjing Old City's extreme population density—captured via real-time modeling including residents, workers, and tourists—amplifies metabolic contributions, unlike studies relying solely on residential data. Secondly, because our study period excludes the heating season, estimated building emissions are lower; in contrast, space heating dominates in colder climates like Basel (60 %; S. Stagakis, Feigenwinter, Vogt & Kalberer, 2023). Thirdly, current high electric vehicle penetration in the study area lowers

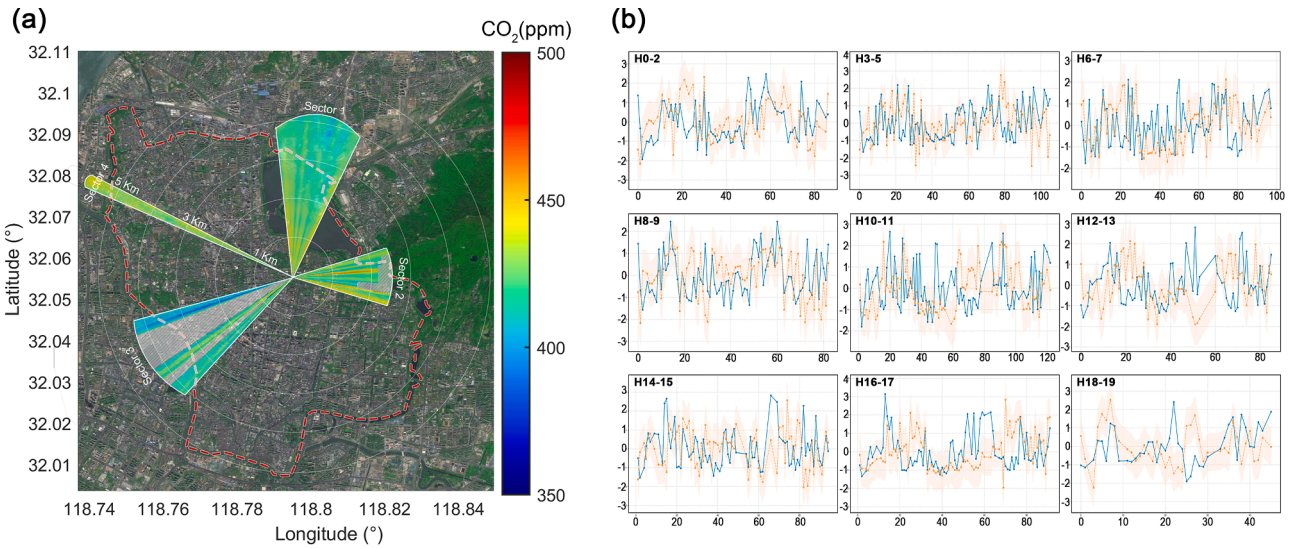

Fig. 12. Comparison of near-surface CO_2 concentrations and simulated emissions. (a) Spatial distribution of LiDAR-observed near-surface CO_2 (ppm) in four azimuthal sectors. (b) Standardized time series of simulated net emissions (blue) and LiDAR-observed near-surface CO_2 (orange), with the shaded ±1 SD envelope around the simulated series.

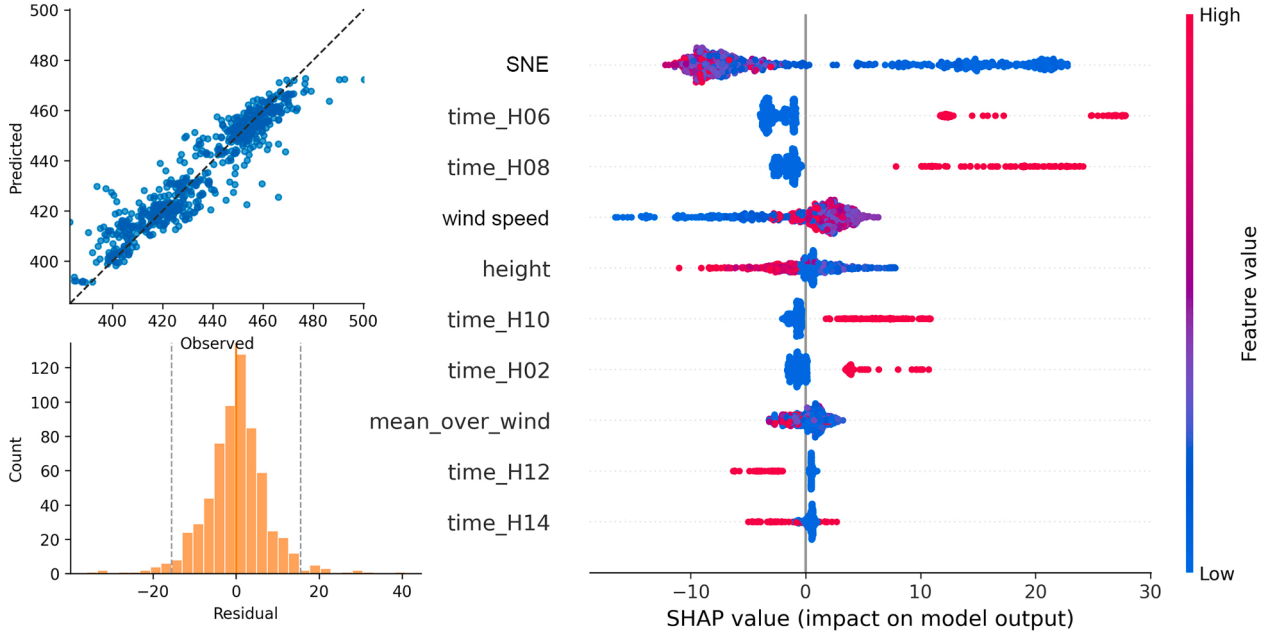

Fig. 13. SHAP summary plot indicating key predictors' relative contribution and directional impact on the near-surface CO_2 concentration.

transport emissions compared to fossil-fuel-dependent cities such as Heraklion (69 %; Stagakis et al., 2019) and London (70 %; Björkegren & Grimmond, 2018). These results underscore how extreme density transforms human respiration into a major carbon source. Although not directly mitigatable, the spatial clustering of metabolic emissions around commercial hubs can guide public service siting, enabling indirect reductions through travel-demand management and spatial optimization (Cai et al., 2022; Wang et al., 2024).

Beyond sectoral composition, diurnal patterns further illuminate urban metabolic rhythms. Building operations exhibited a distinct M-shaped profile, consistent with patterns of synchronized domestic activity observed in studies such as the Hestia project in Indianapolis (Gurney et al., 2012). Transportation emissions were tightly coupled with morning and evening rush hours—a well-documented phenomenon globally, also observed in Beijing (Li et al., 2019; Ye et al., 2023). Our high-resolution temporal data further reveal a significant weekend effect, with traffic emissions decreasing by 18–22 %, underscoring the persistent role of commuting behavior. In contrast, metabolic emissions maintained a daytime plateau, closely tracking pedestrian activity dynamics. These temporal patterns were mirrored in distinct spatial structures. Spatially, emissions exhibited strong clustering: total building emissions were area-driven in peripheral zones, while emission intensity peaked in the dense urban core. Transportation hotspots consistently concentrated at inner-ring road nodes and major gateway corridors, and metabolic fluxes formed multi-center clusters anchored around key commercial areas.

Interactions between diurnal source rhythms and urban spatial structure produce pronounced composite peaks, especially on weekdays. The overlap of morning building start-up loads with inbound commuting yields a strong 07:00–09:00 peak; a second peak at

17:00–19:00 arises when ongoing building operations coincide with outbound traffic. Similar synergies near transport–commercial hubs have been reported (B. Liu et al., 2024; Zhao et al., 2023). Peak sharpness aligns with microenvironmental controls of high-density urban morphology (building thermodynamics, urban heat island, urban CO_2 dome, street-canyon effects) (Idso et al., 2002; Iungman et al., 2024; Liu et al., 2023; Tian et al., 2024). These spatiotemporal dynamics were validated by CDIAL measurements, which provided continuous, spatially representative observations that reduce source-attribution ambiguity and complement existing monitoring networks.

Finally, urban vegetation provided only a minimal carbon sink, offsetting a mere 0.6 % of gross emissions, which is consistent with the limited sequestration (<0.5–7 %) documented in other dense cities (Christen et al., 2011; Havu et al., 2024; S. Stagakis, Feigenwinter, Vogt & Kalberer, 2023; Ye et al., 2023; Ye et al., 2025). This marginal effect, coupled with a spatiotemporal mismatch with emission hotspots, underscores that current urban green spaces cannot meaningfully offset neighborhood-scale peaks without strategic expansion. Nevertheless, concentrated green infrastructure(e.g., Xuanwu Lake Park in Nanjing) can indirectly mitigate emissions by reducing local energy demand through microclimatic regulation (P. Wang et al., 2023), highlighting a broader role for targeted greening in climate-adaptive planning (Bai et al., 2025; Javadpoor et al., 2024).

5.2. Implications for neighborhood-scale decarbonization

The five neighborhood typologies identified (Section 4.1.3) reveal fundamentally distinct carbon emission structures and drivers, underscoring the limitations of citywide one-size-fits-all policies. Instead, decarbonization strategies must be spatially tailored to align with each typology's functional characteristics, emission hotspots, and inherent mitigation potentials. As synthesized in Table 5, targeted, evidence-based interventions are proposed and organized around three interconnected dimensions: spatial planning, technological innovation, and management mechanisms.

For the low-emission neighborhoods, which maintain balanced, minimal emissions across all sectors, the priority is to preserve their low-carbon status while preventing future growth. These areas serve as natural laboratories for replicable practices: distributed renewable microgrids paired with IoT energy monitoring can sustain baseline efficiency (De Loma-Osorio et al., 2024; Duan et al., 2024; Huylo et al., 2025). At the same time, carbon-credit systems incentivize sustainable public service usage without compromising livability (Barrett et al., 2024). By safeguarding their existing low-emission momentum, these neighborhoods can act as anchors for citywide decarbonization.

Table 5
Targeted decarbonization strategies for neighborhood emission typologies.

Typology	Core Challenge	Strategies
Low-emission	Maintaining low-carbon profiles; Avoiding rebound effects	• Spatial: Community renewable microgrids • Tech: IoT energy monitoring + residential electrification • Mgmt.: Carbon-credit schemes
Building-dominated	High fossil dependency (gas); Pronounced diurnal peaks	• Spatial: Rooftop PV + shading • Tech: Smart building controls • Mgmt.: Heat pump subsidies + tiered gas pricing
Mixed high-emission	Spatiotemporal peak synergy; Inadequate carbon sinks	• Spatial: Transit-priority streets + superblocks • Tech: Fleet electrification • Mgmt.: Low-emission zones + optimized freight routing
Transportation-dominated	Morning peak dominance; Road intersection hotspots	• Spatial: Dedicated bus/cycling lanes • Tech: CCUS • Mgmt.: Dynamic congestion pricing
High carbon-sink	Sink-residence spatial mismatch	• Spatial: Blue-green corridor expansion • Tech: Smart irrigation systems • Mgmt.: Ecological protection redlines

Building-dominated neighborhoods are defined by fossil fuel-dependent residential and commercial emissions, requiring targeted retrofits to reduce reliance on non-renewable energy. Rooftop solar integration and enhanced building insulation directly address their primary emission source, while innovative control systems can mitigate usage spikes (Shi et al., 2025; Trencher & van der Heijden, 2019; Zhang et al., 2025). Subsidies for low-carbon heating technologies (e.g., heat pumps) should prioritize these zones, using their moderate emission levels to deliver cost-effective decarbonization.

Mixed high-emission neighborhoods face intertwined challenges from elevated transportation and building emissions, compounded by limited carbon sink capacity. Interventions here must adopt an integrated spatial approach: transit-priority street redesigns and electric fleet deployment can disrupt peak-hour emission synergies (Geels et al., 2017; Yang et al., 2021). At the same time, low-emission zones—modeled after successful implementations in European cities (Borowska-Stefańska et al., 2024, 2025; Moral-Carcedo, 2022; Poulhès & Proulhac, 2021)—can curtail traffic-related emissions. Complementary urban greening measures offset local heat islands and enhance on-site sequestration, addressing the dual drivers of their high emissions (Jia et al., 2025; Priya & Senthil, 2025).

Though small in proportion, transportation-dominated neighborhoods exhibit extreme emission intensity due to concentrated vehicle activity. Spatially, dedicated bus lanes, cycling networks, and pedestrian zones physically reduce private vehicle dependency (Linton et al., 2022); managerially, dynamic congestion pricing targets peak-hour hotspots (Li et al., 2025); and in terms of technology, integrating artificial carbon sink facilities (e.g., CCUS) can locally offset a portion of residual emissions (Rodriguez Mendez et al., 2024; Shang & Lv, 2023).

High carbon-sink neighborhoods play a disproportionate role in urban carbon sequestration, requiring protection and enhancement of their ecological function. Expanding blue-green corridors connects fragmented green spaces within high-density urban environments, amplifying their sequestration potential and aligning sinks with nearby emission sources (Jiang et al., 2023; Song & Wang, 2025). Intelligent irrigation systems maximize vegetation efficiency, while strict ecological redlines prevent urban encroachment. As observed in high-density urban environments globally, these measures preserve their unique capacity to offset emissions, with co-benefits for microclimate regulation (Kumar et al., 2024; Pincetl et al., 2014; Winbourne et al., 2022).

5.3. Limitations and future studies

While the SCE-model provides significant advancements in spatial and temporal granularity, it is essential to acknowledge uncertainties rooted in data, methods, scope, and validation. From a data perspective, because high-resolution traffic probe data are difficult to access, we infer segment-level flows from traffic status indicators using a machine-learning model; however, the available status data are dominated by uncongested periods and may underestimate peak emissions. Although the framework is extensible to the whole year, this analysis is limited to September. It represents emission factors and building schedules with averages, which do not capture seasonal variability and may miss atypical patterns (e.g., holidays, heatwaves, special events).

Several simplifications regarding methods and model structure may affect local accuracy. Uniform building parameters do not reflect within-type heterogeneity in physical characteristics and occupant behavior, potentially biasing estimates in older or highly occupied buildings. At the neighborhood scale, summing sectoral sources does not fully account for interactions among sources or local meteorology, which can decouple emissions from near-surface CO_2.

In terms of scope, the analysis focuses on direct (Scope 1) emissions

from residential, commercial, and transport activities in the high-density study area. Grid electricity generation, industrial point sources, and freight outside primary corridors are excluded. Excluding Scope 2 and 3 underestimates neighborhood carbon footprints but is justified by direct governance relevance.

Regarding validation, near-surface CDIAL is highly precise (±5 ppm), yet in dense urban canyons, its representativeness is curtailed by vertical mixing, building-induced line-of-sight occlusion, and aerosol scattering/absorption. Despite these limitations, the model reproduces diurnal patterns and explains over 79 % of the variance in observed concentrations, supporting its use for fine-scale characterization.

Future studies should focus on: (1) integrating city real-time data streams—linking IoT/smart-meter building energy, dynamic traffic probes and transit feeds, and city operations (events, construction, incidents)—to capture emission peaks and micro-scale variability and enable near-real-time updates; (2) testing and calibrating the framework across additional dense cities with diverse morphologies and climates, and optimizing it using multi-year, multi-season datasets to improve robustness and transferability; (3) expanding the system boundary beyond Scope 1 to explicitly include Scope 2 (indirect electricity) and, where feasible, targeted Scope 3 components for a more complete neighborhood carbon footprint; and (4) building a long-term intra-urban observing network that fuses building-based LiDAR with satellite overpasses, eddy-covariance flux towers, and mobile measurements to enhance calibration, reduce positional bias, and strengthen spatiotemporal representativeness for sustained urban monitoring.

6. Conclusion

This study develops a novel LiDAR-validated spatiotemporal carbon modeling framework (SCE-Model) to address the critical need for high-resolution emission quantification in dense urban neighborhoods, a prerequisite for effective climate change mitigation. By integrating diverse urban datasets (building operations, traffic, human mobility, vegetation dynamics) with near-surface CDIAL measurements (R^2 = 0.79), the framework enables hourly, block-level emission mapping, filling a key gap in actionable urban carbon monitoring.

Applied to Nanjing Old City, this approach reveals three foundational insights into urban carbon dynamics: First, human metabolic activity dominates local emissions, a factor previously underappreciated in dense urban cores. Second, as primary anthropogenic sources, transportation and building emissions exhibit distinct diurnal rhythms and spatial clustering, driving emission hotspots. Third, though concentrated in parks and greenways, urban vegetation sinks provide only modest offsets to these dominant anthropogenic emissions, highlighting a critical sink-source imbalance.

Building on these insights, the framework identifies five distinct neighborhood emission typologies, directly demonstrating the ineffectiveness of citywide “one-size-fits-all” decarbonization policies. Instead, targeted strategies are necessitated by typology-specific characteristics: retrofitting gas-dependent buildings in building-dominated areas; implementing transit-priority streets and low-emission zones in mixed high-emission zones; deploying dedicated bus lanes and congestion pricing in transportation hotspots; and protecting/expanding blue-green corridors in high carbon-sink neighborhoods. As a replicable and validated tool, the SCE-Model provides a transformative approach for high-resolution urban carbon accounting. It strengthens the foundation for evidence-based decarbonization planning and targeted climate action in dense cities globally, offering a scalable pathway to support their transition towards carbon neutrality.

Despite these contributions, this study has several limitations, primarily concerning data granularity, model scope, and seasonal representation. Addressing these limitations presents key avenues for future research. These include the integration of real-time IoT data streams, expansion of the system boundary to encompass Scope 2 and 3 emissions, validation across a wider range of cities and seasons, and the development of a multi-platform urban carbon observing network. By pursuing these directions, the resolution, accuracy, and generalizability of urban carbon accounting can be further enhanced.

CRediT authorship contribution statement

Yueyue Wu: Writing – review & editing, Writing – original draft, Visualization, Validation, Software, Project administration, Methodology, Investigation, Formal analysis, Data curation, Conceptualization. **Yi Zheng:** Writing – review & editing, Resources, Project administration, Methodology, Funding acquisition, Data curation, Conceptualization. **Yixiang Chen:** Writing – review & editing, Validation, Methodology, Investigation, Data curation. **Xinbei Wang:** Writing – review & editing, Visualization, Methodology. **Zhen Zhang:** Writing – review & editing, Validation, Supervision, Methodology, Funding acquisition, Data curation. **Saifen Yu:** Supervision, Methodology, Data curation. **Haiyun Xia:** Supervision, Resources. **ChengHe Guan:** Writing – review & editing, Supervision, Resources, Project administration, Funding acquisition.

Declaration of competing interest

The authors declare that they have no known competing financial interests or personal relationships that could have appeared to influence the work reported in this paper.

Acknowledgments

This research is funded by the National Natural Science Foundation of China, grant number 52394224; Open Fund Project of the Key Laboratory of Ecology and Energy Saving Study of Dense Habitat, Ministry of Education, grant number 20240110; The Young Elite Scientists Sponsorship Program by China Association for Science and Technology, grant number 2022QNRC001-YESS20220569; Shanghai Key Laboratory of Urban Design and Urban Science, NYU Shanghai Open Topic Grants, grant number 2023YZheng_LOUD; Natural Science Foundation of Jiangsu Province, grant number BK20230428; the Shanghai Nature and Health Foundation (Grant No 20230701 SNHF), Shanghai, China; Pudong Pearl Program Leading Scheme 2023, Pudong Talents Office; Program for Professor of Special Appointment (Eastern Scholar) at Shanghai Institutions of Higher Learning (Grant No 20230111 SMEC); National Foreign Young Talents Program from the State Administration of Foreign Experts Affairs (Grant No 10109_Special Grant); Shanghai Municipal Education Commission (Key program of AI-Driven Initiative to Promote Research Paradigm Reform and Empower Disciplinary Advancement) (Grant No. 20240101B SMEC CH_Guan). The authors would like to grateful to the editor and anonymous reviewers for their positive comments on the manuscript.

Supplementary materials

Supplementary material associated with this article can be found, in the online version, at doi:10.1016/j.scs.2025.106981.

Data availability

Data will be made available on request.

References

Amjath-Babu, T. S., Anwar, N. H., Chanda, A., Chaturvedi, R. K., Hina, S., Fadnavis, S., Sarathchandra, C., Shakya, S. R., & Singh, C. (2025). Perspectives on climate change in South Asia. *Nature Climate Change, 15*(10), 1025–1030. https://doi.org/10.1038/s41558-025-02442-7

Apte, J. S., & Manchanda, C. (2024). High-resolution urban air pollution mapping. *Science (New York, N.Y.), 385*(6707), 380–385. https://doi.org/10.1126/science.adq3678

Bai, X., Fu, X., Ren, Z., Auffrey, C., & Wang, Q. (2025). Retrofitting green spaces based on dispersion and absorption of mobile-source carbon emissions. *Transportation Research Part D: Transport and Environment, 146*, Article 104874. https://doi.org/10.1016/j.trd.2025.104874

Barrett, B. F. D., Trencher, G. P., Truong, N., & Ohta, H. (2024). How can cities achieve accelerated systemic decarbonization? Analysis of six frontrunner cities. *Sustainable Cities and Society, 100*, Article 105000. https://doi.org/10.1016/j.scs.2023.105000

Björkegren, A., & Grimmond, C. (2018). Net carbon dioxide emissions from central London. *Urban Climate, 23*, 131–158. https://doi.org/10.1016/j.uclim.2016.10.002

Borowska-Stefańska, M., Dulebenets, M. A., Sahebgharani, A., Wiśniewski, S., & Kozieł, M. (2024). Evaluating low-emission-zone impacts on urban road transport system in large city. *Transportation Research Part D: Transport and Environment, 137*, Article 104503. https://doi.org/10.1016/j.trd.2024.104503

Borowska-Stefańska, M., Dulebenets, M. A., Sahebgharani, A., & Wiśniewski, S. (2025). Periodic low emission zones: balancing urban transport efficiency and reducing traffic emissions. *Cities (London, England), 163*, Article 106005. https://doi.org/10.1016/j.cities.2025.106005

Brown, W., & MacAskill, K. (2025). Accounting and management of city carbon emissions: Trajectories towards advanced data use. *Sustainable Cities and Society, 131*, 106677. https://doi.org/10.1016/j.scs.2025.106677

Cai, B., Liang, S., Zhou, J., Wang, J., Cao, L., Qu, S., Xu, M., & Yang, Z. (2018). China high resolution emission database (CHRED) with point emission sources, gridded emission data, and supplementary socioeconomic data. *Resources, Conservation and Recycling, 129*, 232–239. https://doi.org/10.1016/j.resconrec.2017.10.036

Cai, Q., Zeng, N., Zhao, F., Han, P., Liu, D., Lin, X., & Chen, J. (2022). The impact of human and livestock respiration on CO2 emissions from 14 global cities. *Carbon Balance and Management, 17*(1), 17. https://doi.org/10.1186/s13021-022-00217-7

Chen, T., & Debnath, R. (2025). The need of explainability in low-carbon urban system design using AI: A systematic review. *Machine Learning: Earth, 1*(1), Article 011001. https://doi.org/10.1088/3049-4753/adde60

Chen, Y., Wang, Z., Wen, Q., Meng, J., Huo, J., Li, S., Zhou, L., Chen, P., Liang, D., Bi, J., & Guan, D. (2025). A building-scale modeling framework for urban net-zero transitions in Nanjing. *Nature Communications, 16*(1), 8954. https://doi.org/10.1038/s41467-025-64016-7

Christen, A., Coops, N. C., Crawford, B. R., Kellett, R., Liss, K. N., Olchovski, I., Tooke, T. R., van der Laan, M., & Voogt, J. A. (2011). Validation of modeled carbon-dioxide emissions from an urban neighborhood with direct eddy-covariance measurements. *Atmospheric Environment, 45*(33), 6057–6069. https://doi.org/10.1016/j.atmosenv.2011.07.040

Christen, A. (2014). Atmospheric measurement techniques to quantify greenhouse gas emissions from cities. *Urban Climate, 10*, 241–260. https://doi.org/10.1016/j.uclim.2014.04.006

Cui, L., Yang, H., Martin, M., Qiao, Y., Ulrich, V., & Zipf, A. (2025). Mapping high-resolution carbon emission spatial distribution combined with carbon satellite and muti-source data. *Remote Sensing, 17*(17), 3125. https://doi.org/10.3390/rs17173125

De Loma-Osorio, I., Borge-Diez, D., Herskind Sejr, J., & Rosales-Asensio, E. (2024). Enhancing commercial building resiliency through microgrids with distributed energy sources and battery energy storage systems. *Energy and Buildings, 325*, Article 114980. https://doi.org/10.1016/j.enbuild.2024.114980

Dou, X., Wang, Y., Ciais, P., Chevallier, F., Davis, S. J., Crippa, M., Janssens-Maenhout, G., Guizzardi, D., Solazzo, E., Yan, F., Huo, D., Zheng, B., Zhu, B., Cui, D., Ke, P., Sun, T., Wang, H., Zhang, Q., Gentine, P., & Liu, Z. (2022). Near-real-time global gridded daily CO2 emissions. *The Innovation, 3*(1), Article 100182. https://doi.org/10.1016/j.xinn.2021.100182

Duan, Y., Li, L., Rezaee Jordehi, A., Tostado-Véliz, M., & Safaraliev, M. (2024). A hierarchical framework for integration of smart buildings in fully-renewable multi-microgrids and distribution systems: towards more sustainable societies. *Sustainable Cities and Society, 115*, Article 105800. https://doi.org/10.1016/j.scs.2024.105800

Fichera, A., Inturri, G., La Greca, P., & Palermo, V. (2016). A model for mapping the energy consumption of buildings, transport and outdoor lighting of neighbourhoods. *Cities (London, England), 55*, 49–60. https://doi.org/10.1016/j.cities.2016.03.011

Gao, F., Wu, J., Xiao, J., Li, X., Liao, S., & Chen, W. (2023). Spatially explicit carbon emissions by remote sensing and social sensing. *Environmental Research, 221*, Article 115257. https://doi.org/10.1016/j.envres.2023.115257

Geels, F. W., Sovacool, B. K., Schwanen, T., & Sorrell, S. (2017). Sociotechnical transitions for deep decarbonization. *Science (New York, N.Y.), 357*(6357), 1242–1244. https://doi.org/10.1126/science.aao3760

Goret, M., Masson, V., Schoetter, R., & Moine, M.-P. (2019). Inclusion of CO2 flux modelling in an urban canopy layer model and an evaluation over an old European city centre. *Atmospheric Environment: X, 3*, Article 100042. https://doi.org/10.1016/j.aeaoa.2019.100042

Guevara, M., Martínez, F., Arévalo, G., Gassó, S., & Baldasano, J. M. (2013). An improved system for modelling Spanish emissions: HERMESv2.0. *Atmospheric Environment, 81*, 209–221. https://doi.org/10.1016/j.atmosenv.2013.08.053

Gurney, K. R., Razlivanov, I., Song, Y., Zhou, Y., Benes, B., & Abdul-Massih, M. (2012). Quantification of fossil fuel CO2 emissions on the building/street scale for a large US City. *Environmental Science & Technology, 46*(21), 12194–12202. https://doi.org/10.1021/es3011282

Gurney, K. R., Liang, J., O'Keeffe, D., Patarasuk, R., Hutchins, M., Huang, J., Rao, P., & Song, Y. (2019). Comparison of global downscaled versus bottom-up fossil fuel CO_2 emissions at the urban scale in four US urban areas. *Journal of Geophysical Research-Atmospheres, 124*(5), 2823–2840. https://doi.org/10.1029/2018JD028859

Gurney, K. R., Liang, J., Roest, G., Song, Y., Mueller, K., & Lauvaux, T. (2021). Under-reporting of greenhouse gas emissions in U.S. cities. *Nature Communications, 12*(1), 553. https://doi.org/10.1038/s41467-020-20871-0

Havu, M., Kulmala, L., Lee, H. S., Saranko, O., Soininen, J., Ahongshangbam, J., & Järvi, L. (2024). CO2 uptake of urban vegetation in a warming Nordic city. *Urban Forestry & Urban Greening, 94*, Article 128261. https://doi.org/10.1016/j.ufug.2024.128261

Hu, K., Zhang, Q., Gong, S., Zhang, F., Weng, L., Jiang, S., & Xia, M. (2024). A review of anthropogenic ground-level carbon emissions based on satellite data. *IEEE Journal of Selected Topics in Applied Earth Observations and Remote Sensing, 17*, 8339–8357. https://doi.org/10.1109/JSTARS.2024.3355549

Huylo, M., Taheri, S., & Novoselac, A. (2025). Integration of renewable energy generation and storage systems for emissions reduction in an islanded campus microgrid. *Building and Environment, 274*, Article 112736. https://doi.org/10.1016/j.buildenv.2025.112736

Idso, S. B., Idso, C. D., & Balling, R. C. (2002). Seasonal and diurnal variations of near-surface atmospheric CO2 concentration within a residential sector of the urban CO2 dome of Phoenix, AZ, USA. *Atmospheric Environment, 36*(10), 1655–1660. https://doi.org/10.1016/S1352-2310(02)00159-0

Intergovernmental Panel on Climate Change (IPCC). (2022). *Contribution of working group III to the sixth assessment report of the intergovernmental panel on climate change*. IPCC. https://report.ipcc.ch/ar6wg3/pdf/IPCC_AR6_WGIII_SummaryForPolicymakers.pdf.

Iungman, T., Khomenko, S., Barboza, E. P., Cirach, M., Gonçalves, K., Petrone, P., Erbertseder, T., Taubenböck, H., Chakraborty, T., & Nieuwenhuijsen, M. (2024). The impact of urban configuration types on urban heat islands, air pollution, CO2 emissions, and mortality in Europe: A data science approach. *The Lancet Planetary Health, 8*(7), e489–e505. https://doi.org/10.1016/S2542-5196(24)00120-7

Järvi, L., Havu, M., Ward, H. C., Bellucco, V., McFadden, J. P., Toivonen, T., Heikinheimo, V., Kolari, P., Riikonen, A., & Grimmond, C. S. B (2019). Spatial modeling of local-scale biogenic and anthropogenic carbon dioxide emissions in Helsinki. *Journal of Geophysical Research: Atmospheres, 124*(15), 8363–8384. https://doi.org/10.1029/2018JD029576

Javadpoor, M., Sharifi, A., & Gurney, K. R. (2024). Mapping the relationship between urban form and CO2 emissions in three US cities using the Local Climate Zones (LCZ) framework. *Journal of Environmental Management, 370*, Article 122723. https://doi.org/10.1016/j.jenvman.2024.122723

Jia, X., Song, P., Liu, Y., He, R., Tian, G., Ge, S., & Lei, Y. (2025). Managing urban parks to unlock carbon sequestration potential: active LiDAR and machine learning approach. *Urban Forestry & Urban Greening, 112*, Article 128996. https://doi.org/10.1016/j.ufug.2025.128996

Jiang, Y., Sun, Y., Liu, Y., & Li, X. (2023). Exploring the correlation between waterbodies, green space morphology, and carbon dioxide concentration distributions in an urban waterfront green space: A simulation study based on the carbon cycle. *Sustainable Cities and Society, 98*, Article 104831. https://doi.org/10.1016/j.scs.2023.104831

Kellett, R., Christen, A., Coops, N. C., van der Laan, M., Crawford, B., Tooke, T. R., & Olchovski, I. (2013). A systems approach to carbon cycling and emissions modeling at an urban neighborhood scale. *Landscape and Urban Planning, 110*, 48–58. https://doi.org/10.1016/j.landurbplan.2012.10.002

Koch, G. J., Barnes, B. W., Petros, M., Beyon, J. Y., Amzajerdian, F., Yu, J., Davis, R. E., Ismail, S., Vay, S., Kavaya, M. J., & Singh, U. N. (2004). Coherent differential absorption lidar measurements of CO_2. *Applied Optics, 43*(26), 5092–5099. https://doi.org/10.1364/AO.43.005092

Kumar, P., Debele, S. E., Khalili, S., Halios, C. H., Sahani, J., Aghamohammadi, N., Andrade, M., de, F., Athanassiadou, M., Bhui, K., Calvillo, N., Cao, S.-J., Coulon, F., Edmondson, J. L., Fletcher, D., Dias de Freitas, E., Guo, H., Hort, M. C., Katti, M., Kjeldsen, T. R., & Jones, L. (2024). Urban heat mitigation by green and blue infrastructure: drivers, effectiveness, and future needs. *The Innovation, 5*(2), Article 100588. https://doi.org/10.1016/j.xinn.2024.100588

Li, Y., Zheng, J., Dong, S., Wen, X., Jin, X., Zhang, L., & Peng, X. (2019). Temporal variations of local traffic CO2 emissions and its relationship with CO2 flux in Beijing, China. *Transportation Research Part D: Transport and Environment, 67*, 1–15. https://doi.org/10.1016/j.trd.2018.10.007

Li, J., Zhang, Y., Yu, S., Qin, H., & Xu, Z. (2025). AI-driven urban planning optimization: A graph neural network and genetic algorithm framework for tackling peak-hour challenges. *Sustainable Cities and Society, 126*, Article 106407. https://doi.org/10.1016/j.scs.2025.106407

Lian, J., Lauvaux, T., Utard, H., Bréon, F.-M., Broquet, G., Ramonet, M., Laurent, O., Albarus, I., Chariot, M., Kotthaus, S., Haeffelin, M., Sanchez, O., Perrussel, O., Denier van der Gon, H. A., Dellaert, S. N. C., & Ciais, P. (2023). Can we use atmospheric CO_2 measurements to verify emission trends reported by cities? Lessons from a 6-year atmospheric inversion over Paris. *Atmospheric Chemistry and Physics, 23*(15), 8823–8835. https://doi.org/10.5194/acp-23-8823-2023

Linton, S., Clarke, A., & Tozer, L. (2022). Technical pathways to deep decarbonization in cities: eight best practice case studies of transformational climate mitigation. *Energy Research & Social Science, 86*, Article 102422. https://doi.org/10.1016/j.erss.2021.102422

Liu, B., Li, F., Hou, Y., Antonio Biancardo, S., & Ma, X. (2024a). Unveiling built environment impacts on traffic CO2 emissions using Geo-CNN weighted regression. *Transportation Research Part D: Transport and Environment, 132*, Article 104266. https://doi.org/10.1016/j.trd.2024.104266

Liu, Z., Zhong, J., Liu, Y., Liang, Y., & Li, Z. (2024b). Dynamic simulation of street-level carbon emissions in megacities: A case study of Wuhan City, China (2015–2030). *Sustainable Cities and Society, 115*, Article 105853. https://doi.org/10.1016/j.scs.2024.105853

Liu, W., Liu, L., Gui, X., Hu, J., & Zheng, Z. (2025). Exploring the impacts from residence characteristics on household carbon emission: the evidence from building image data. *Energy and Buildings, 347*, Article 116263. https://doi.org/10.1016/j.enbuild.2025.116263

Liu, S., Kwok, Y. T., & Ren, C. (2023). Investigating the impact of urban microclimate on building thermal performance: A case study of dense urban areas in Hong Kong. *Sustainable Cities and Society, 94*, Article 104509. https://doi.org/10.1016/j.scs.2023.104509

Luo, H., Li, Y., Gao, X., Meng, X., Yang, X., & Yan, J. (2023). Carbon emission prediction model of prefecture-level administrative region: A land-use-based case study of Xi'an city, China. *Applied Energy, 348*, Article 121488. https://doi.org/10.1016/j.apenergy.2023.121488

Luo, W.-R., Che, H.-Z., Miao, S.-G., Dou, J.-X., Zheng, Y.-Q., Zhou, Y.-Y., Su, Z.-M., Wu, Y., Wang, D., Yi, X., Gui, K., Zheng, Y., Li, L., & Zhang, X.-Y. (2025). Simulation of CO2 flux and evaluation of carbon neutrality potential at the neighborhood scale in Beijing with multi-source data. *Advances in Climate Change Research, 16*(5), 1070–1086. https://doi.org/10.1016/j.accre.2025.06.008

Mi, Z., Guan, D., Liu, Z., Liu, J., Viguie, V., Fromer, N., & Wang, Y. (2019). Cities: the core of climate change mitigation. *Journal of Cleaner Production, 207*, 582–589. https://doi.org/10.1016/j.jclepro.2018.10.034

Montfort, S., Callaghan, M., Creutzig, F., Lamb, W. F., Lu, C., Repke, T., Ge, K., & Minx, J. (2025). Systematic global stocktake of over 50,000 urban climate change studies. *Nature Cities, 2*(7), 613–625. https://doi.org/10.1038/s44284-025-00260-8

Moral-Carcedo, J. (2022). Dissuasive effect of low emission zones on traffic: the case of Madrid Central. *Transportation, 51*(1), 25–49. https://doi.org/10.1007/s11116-022-10318-4

Moriwaki, R., & Kanda, M. (2004). Seasonal and diurnal fluxes of radiation, heat, water vapor, and carbon dioxide over a suburban area. *Journal of Applied Meteorology, 43*(11), 1700–1710. https://doi.org/10.1175/JAM2153.1

Mueller, K. L., Lauvaux, T., Gurney, K. R., Roest, G., Ghosh, S., Gourdji, S. M., Karion, A., DeCola, P., & Whetstone, J. (2021). An emerging GHG estimation approach can help cities achieve their climate and sustainability goals. *Environmental Research Letters, 16*(8), Article 084003. https://doi.org/10.1088/1748-9326/ac0f25

Pincetl, S., Chester, M., Circella, G., Fraser, A., Mini, C., Murphy, S., Reyna, J., & Sivaraman, D. (2014). Enabling future sustainability transitions an urban metabolism approach to Los Angeles. *Journal of Industrial Ecology, 18*(6), 871–882. https://doi.org/10.1111/jiec.12144

Poulhès, A., & Proulhac, L. (2021). The Paris Region low emission zone, a benefit shared with residents outside the zone. *Transportation Research Part D: Transport and Environment, 98*, Article 102977. https://doi.org/10.1016/j.trd.2021.102977

Priya, U. K., & Senthil, R. (2025). Enhancing sustainable urban planning to mitigate urban heat island effects through residential greening. *Sustainable Cities and Society, 129*, Article 106512. https://doi.org/10.1016/j.scs.2025.106512

Rodriguez Mendez, Q., Fuss, S., Lück, S., & Creutzig, F. (2024). Assessing global urban CO2 removal. *Nature Cities, 1*(6), 413–423. https://doi.org/10.1038/s44284-024-00069-x

Shang, W.-L., & Lv, Z. (2023). Low carbon technology for carbon neutrality in sustainable cities: A survey. *Sustainable Cities and Society, 92*, Article 104489. https://doi.org/10.1016/j.scs.2023.104489

Shi, M., Lu, X., & Craig, M. T. (2025). Unveiling deployable rooftop solar potential across Chinese cities. *Nature Cities, 2*(7), 650–661. https://doi.org/10.1038/s44284-025-00270-6

Sm, S. N., Reddy Yasa, P., Mv, N., Khadirnaikar, S., & Rani, Pooja (2019). Mobile monitoring of air pollution using low cost sensors to visualize spatio-temporal variation of pollutants at urban hotspots. *Sustainable Cities and Society, 44*, 520–535. https://doi.org/10.1016/j.scs.2018.10.006

Song, H., & Wang, M. (2025). Integrating ecosystem services: A new indicator for evaluating net carbon sink efficiency of urban green spaces and its influencing factors. *Ecological Indicators, 178*, Article 113901. https://doi.org/10.1016/j.ecolind.2025.113901

Stagakis, S., Chrysoulakis, N., Spyridakis, N., Feigenwinter, C., & Vogt, R. (2019). Eddy covariance measurements and source partitioning of CO2 emissions in an urban environment: application for Heraklion, Greece. *Atmospheric Environment, 201*, 278–292. https://doi.org/10.1016/j.atmosenv.2019.01.009

Stagakis, S., Feigenwinter, C., Vogt, R., Brunner, D., & Kalberer, M. (2023). A high-resolution monitoring approach of urban CO2 fluxes. Part 2-surface flux optimisation using eddy covariance observations. *Science of the Total Environment, 903*, Article 166035. https://doi.org/10.1016/j.scitotenv.2023.166035

Stagakis, S., Feigenwinter, C., Vogt, R., & Kalberer, M. (2023). A high-resolution monitoring approach of urban CO2 fluxes. Part 1-bottom- up model development. *Science of the Total Environment, 858*, Article 160216. https://doi.org/10.1016/j.scitotenv.2022.160216

Tian, P., Cai, M., Sun, Z., Liu, S., Wu, H., Liu, L., & Peng, Z. (2024). Effects of 3D urban morphology on CO2 emissions using machine learning: towards spatially tailored low-carbon strategies in Central Wuhan, China. *Urban Climate, 57*, Article 102122. https://doi.org/10.1016/j.uclim.2024.102122

Trencher, G., & van der Heijden, J. (2019). Instrument interactions and relationships in policy mixes: achieving complementarity in building energy efficiency policies in New York, Sydney and Tokyo. *Energy Research & Social Science, 54*, 34–45. https://doi.org/10.1016/j.erss.2019.02.023

Ueyama, M., & Takano, T. (2022). A decade of CO2 flux measured by the eddy covariance method including the COVID-19 pandemic period in an urban center in Sakai, Japan. *Environmental Pollution, 304*, Article 119210. https://doi.org/10.1016/j.envpol.2022.119210

United Nations Human Settlements Programme (UN-Habitat). (2022). World Cities Report 2022: Envisaging the future of cities. Nairobi: UN-Habitat. Retrieved November 18, 2025, from https://unhabitat.org/wcr/2022/.

Velasco, E. (2021). Impact of Singapore's COVID-19 confinement on atmospheric CO2 fluxes at neighborhood scale. *Urban Climate, 37*, Article 100822. https://doi.org/10.1016/j.uclim.2021.100822

Wang, P., Zhou, W., Niu, Z., Huo, D., Zhou, J., Li, H., Cheng, P., Wu, S., Xiong, X., & Chen, N. (2024). An approach for assessing Human respiration CO2 emissions using radiocarbon measurements and bottom-up data sets. *Journal of Geophysical Research: Atmospheres, 129*(9), Article e2023JD040578. https://doi.org/10.1029/2023JD040578

Wang, T., Yan, F., Ma, J., Zhang, X., & Dong, L. (2025). Using a machine learning framework for natural language processing to create a high-resolution carbon emission map for urban manufacturing. *Environment and Planning B: Urban Analytics and City Science*. , Article 23998083241312948. https://doi.org/10.1177/23998083241312948

Wang, G., Han, Q., & de Vries, B. (2020). A geographic carbon emission estimating framework on the City scale. *Journal of Cleaner Production, 244*, Article 118793. https://doi.org/10.1016/j.jclepro.2019.118793

Wang, Y., Wang, M., Teng, F., & Ji, Y. (2023). Remote sensing monitoring and analysis of spatiotemporal changes in China's anthropogenic carbon emissions based on XCO2 data. *Remote Sensing, 15*(12), 3207. https://doi.org/10.3390/rs15123207

Wang, P., Yang, Y., Ji, C., & Huang, L. (2023). Positivity and difference of influence of built environment around urban park on building energy consumption. *Sustainable Cities and Society, 89*, Article 104321. https://doi.org/10.1016/j.scs.2022.104321

Winbourne, J. B., Smith, I. A., Stoynova, H., Kohler, C., Gately, C. K., Logan, B. A., Reblin, J., Reinmann, A., Allen, D. W., & Hutyra, L. R. (2022). Quantification of urban forest and grassland carbon fluxes using field measurements and a satellite-based model in Washington DC/Baltimore area. *Journal of Geophysical Research: Biogeosciences, 127*(1), Article e2021JG006568. https://doi.org/10.1029/2021JG006568

Wu, Y., Zheng, Y., Liu, J., Yang, Q., Shi, B., Guan, C., & Deng, W. (2025). Spatial and temporal variability of near-surface CO2 and influencing factors in urban communities. *Land, 14*(4), 888. https://doi.org/10.3390/land14040888

Yang, X., Lin, W., Gong, R., Zhu, M., & Springer, C. (2021). Transport decarbonization in big cities: an integrated environmental co-benefit analysis of vehicles purchases quota-limit and new energy vehicles promotion policy in Beijing. *Sustainable Cities and Society, 71*, Article 102976. https://doi.org/10.1016/j.scs.2021.102976

Yap, W., Wu, A. N., Miller, C., & Biljecki, F. (2025). Revealing building operating carbon dynamics for multiple cities. *Nature Sustainability, 8*(10), 1199–1210. https://doi.org/10.1038/s41893-025-01615-8

Ye, H., Li, Y., Shi, D., Meng, D., Zhang, N., & Zhao, H. (2023). Evaluating the potential of achieving carbon neutrality at the neighborhood scale in urban areas. *Sustainable Cities and Society, 97*, Article 104764. https://doi.org/10.1016/j.scs.2023.104764

Ye, X., Wang, Z., Cui, K., Meng, S., & Ning, X. (2025). Data-driven neighborhood-level carbon emission accounting models and decarbonization strategies: empirical study on Central Shenyang City. *Sustainable Cities and Society, 125*, Article 106346. https://doi.org/10.1016/j.scs.2025.106346

Yu, S., Zhang, Z., Xia, H., Dou, X., Wu, T., Hu, Y., Li, M., Shangguan, M., Wei, T., Zhao, L., Wang, L., Jiang, P., Zhang, C., You, L., Tao, L., & Qiu, J. (2021). Photon-counting distributed free-space spectroscopy. *Light: Science & Applications, 10*(1), 212. https://doi.org/10.1038/s41377-021-00650-2

Yu, S., Guo, K., Li, S., Han, H., Zhang, Z., & Xia, H. (2024). Three-dimensional detection of CO_2 and wind using a 1.57 μm coherent differential absorption lidar. *Optics Express, 32*(12), 21134–21148. https://doi.org/10.1364/OE.523904

Yue, B., Yu, S., Li, M., Wei, T., Yuan, J., Zhang, Z., Dong, J., Jiang, Y., Yang, Y., Gao, Z., & Xia, H. (2022). Local-scale horizontal CO2 flux estimation incorporating differential absorption lidar and coherent doppler wind lidar. *Remote Sensing, 14*(20), Article 20. https://doi.org/10.3390/rs14205150

Zhang, Z., Qian, Z., Chen, M., Zhu, R., Zhang, F., Zhong, T., Lin, J., Ning, L., Xie, W., Creutzig, F., Tang, W., Liu, L., Yang, J., Pu, Y., Cai, W., Pu, Y., Liu, D., Yang, H., Su, H., & Yan, J. (2025). Worldwide rooftop photovoltaic electricity generation may mitigate global warming. *Nature Climate Change, 15*(4), 393–402. https://doi.org/10.1038/s41558-025-02276-3

Zhao, C., & Jiao, H. (2024). Estimating the marginal effects of plot-scale socio-economic and spatial morphological factors on carbon emissions from non-linear perspective. *Journal of Cleaner Production, 484*, Article 144318. https://doi.org/10.1016/j.jclepro.2024.144318

Zhao, C., Tang, J., Zeng, Y., Li, Z., & Gao, F. (2023). Understanding the spatio-temporally heterogeneous effects of built environment on urban travel emissions. *Journal of Transport Geography, 112*, Article 103689. https://doi.org/10.1016/j.jtrangeo.2023.103689

Zheng, Y., Li, W., Jiang, L., Yuan, C., Xiao, T., Wang, R., Cai, M., & Hong, H. (2024). Spatial modelling of street-level carbon emissions with multi-source open data: A case study of Guangzhou. *Urban Climate, 55*, Article 101974. https://doi.org/10.1016/j.uclim.2024.101974

Zhu, X.-H., Lu, K.-F., Peng, Z.-R., He, H.-D., & Xu, S.-Q. (2022). Spatiotemporal variations of carbon dioxide (CO2) at urban neighborhood scale: characterization of distribution patterns and contributions of emission sources. *Sustainable Cities and Society, 78*, Article 103646. https://doi.org/10.1016/j.scs.2021.103646